NEUROSCIENCE

WiChR, a highly potassium-selective channelrhodopsin for low-light one- and two-photon inhibition of excitable cells

Johannes Vierock[1,2]*†, Enrico Peter[1]†, Christiane Grimm[3]†, Andrey Rozenberg[4], I-Wen Chen[3], Linda Tillert[2], Alejandro G. Castro Scalise[1], Marilù Casini[5,6], Sandra Augustin[1], Dimitrii Tanese[3], Benoît C. Forget[3], Rémi Peyronnet[5], Franziska Schneider-Warme[5], Valentina Emiliani[3], Oded Béjà[4], Peter Hegemann[1]*

The electric excitability of muscle, heart, and brain tissue relies on the precise interplay of Na^+- and K^+-selective ion channels. The involved ion fluxes are controlled in optogenetic studies using light-gated channelrhodopsins (ChRs). While non-selective cation-conducting ChRs are well established for excitation, K^+-selective ChRs (KCRs) for efficient inhibition have only recently come into reach. Here, we report the molecular analysis of recently discovered KCRs from the stramenopile *Hyphochytrium catenoides* and identification of a novel type of hydrophobic K^+ selectivity filter. Next, we demonstrate that the KCR signature motif is conserved in related stramenopile ChRs. Among them, WiChR from *Wobblia lunata* features a so far unmatched preference for K^+ over Na^+, stable photocurrents under continuous illumination, and a prolonged open-state lifetime. Showing high expression levels in cardiac myocytes and neurons, WiChR allows single- and two-photon inhibition at low irradiance and reduced tissue heating. Therefore, we recommend WiChR as the long-awaited efficient and versatile optogenetic inhibitor.

INTRODUCTION

Light-gated ion channels are used in modern life sciences from plant physiology to systems neuroscience to control the electrical activity of cells noninvasively with the temporal and spatial precision of light (*1*). Simultaneous illumination of individual cells within larger brain areas is reliably achieved by holographic light shaping and two-photon (2P) excitation (*2*). The used light switches are in most cases channelrhodopsins (ChRs) that absorb light via a retinal chromophore bound to the seven-transmembrane helix protein. First described as the photoreceptor responsible for phototaxis in the green alga *Chlamydomonas reinhardtii* (*3*), ChRs have been discovered across different groups of unicellular organisms-with close to 800 representatives known today (*4*, *5*).

While cation-conducting ChRs (CCRs) are well established for excitation, neuronal inhibition is most frequently achieved with anion-conducting ChRs (ACRs). However, variability of internal Cl^- concentration in subcellular neuronal compartments, in cardiomyocytes (CMs), and during development, may cause depolarization instead of hyperpolarization and limits the application of ACRs (*6*–*8*). Other inhibitory tools, such as light-driven ion pumps and inhibitory $G_{i/o}$-coupled opto-GPCRs (G protein–coupled receptors), also have substantial limitations. Optogenetic pumps require high expression levels and continuous bright illumination due to a strict one photon/one charge ratio and can have undesired side effects (*9*). Opto-GPCRs require cell type–specific examination of engaged signaling cascades and might activate multiple signaling pathways with limited temporal on-off control (*10*).

An attractive alternative for optogenetic inhibition and a long-sought tool is a K^+-selective CCR that would hyperpolarize the cellular membrane despite high extracellular Na^+ concentration and mimic the major endogenous repolarization processes based on K^+ efflux. Engineering a K^+-selective ChR has been an ambitious goal, considering the low structural similarity between ChRs and natural K^+ channels, and was unsuccessful so far. ChRs conduct protons and partly hydrated ions along a sequence of water-filled cavities through an asymmetric and still structurally unknown pore within a rhodopsin monomer (*11*). Mammalian K^+ channels feature a highly conserved and symmetric selectivity filter with four subsequent K^+ binding sites for K^+ dehydration in the symmetry axis of the tetrameric channel (*12*). Accordingly, first-generation K^+ channels combined light-sensitive modules, such as ultraviolet-switchable azobenzene compounds, blue light–sensitive light-oxygen-voltage sensing (LOV) domains, or blue light–activated cyclases with ligand-, viral-, and adenosine 3′,5′-monophosphate (cAMP)–gated K^+ channels, as single- or two-component systems (*13*–*15*). Currently, the need for an additional cofactor, low expression, slow kinetics, a limited dynamic range, and putative side effects have limited their application . Structure-guided molecular engineering of ChRs led to only minor improvements in the P_{K+}/P_{Na+} permeability ratio (*11*), whereas modification of the extracellular release channel of the light-driven Na^+ pump KR2 of *Dokdonia eikasta* unexpectedly generated an operational light-activated K^+ channel with substantial K^+ conductance. However, the

[1]Institut für Biologie, Experimentelle Biophysik, Humboldt-Universität zu Berlin, Berlin, Germany. [2]Neuroscience Research Center, Charité–Universitätsmedizin Berlin, Berlin, Germany. [3]Wavefront Engineering Microscopy Group, Photonics Department, Institut de la Vision, Sorbonne Université, INSERM, CNRS, Paris, France. [4]Faculty of Biology, Technion–Israel Institute of Technology, Haifa 32000, Israel. [5]Institute for Experimental Cardiovascular Medicine, University Heart Center Freiburg · Bad Krozingen, Medical Center and Faculty of Medicine, University of Freiburg, Freiburg im Breisgau, Germany. [6]Regenerative Medicine and Heart Transplantation Unit, Instituto de Investigación Sanitaria La Fe and ITACA Institute (COR), Universitat Politècnica de València, Valencia, Spain.
†These authors contributed equally to this work.
*Corresponding author: johannes.vierock@charite.de (J.V.); hegemann@rz.hu-berlin.de (P.H.)

conductance was only large enough as needed for application at alkaline pH (*16*).

Another milestone was achieved with the recent discovery of two natural K^+-conducting ChRs (KCRs) in the stramenopile *Hyphochytrium catenoides* (HcKCR1 and HcKCR2) that were K^+ selective enough to inhibit action potential (AP) firing in neuronal slices (*17*). Both KCRs have a bacteriorhodopsin-like DTD motif in membrane helix 3 (D85, T89, and D96 in bacteriorhodopsin). This is a feature shared with the related cryptophyte CCRs that were first discovered in *Guillardia theta* (*18*) and that include the green light–activated nonselective cation channel ChRmine from *Rhodomonas lens*, the structure of which was recently solved by cryo–electron microscopy (*19*, *20*). Despite a thorough initial characterization by Govorunova and colleagues (*17*), the molecular determinants of K^+ selectivity in this just recently identified group of KCRs remain unknown.

Here, we characterize the K^+ selectivity of both HcKCRs, quantify their residual Na^+ conductance, and identify key residues for K^+ conductance and selection over Na^+. A search for further CCRs containing the identified K^+ selectivity signature motif revealed WiChR, a KCR from *Wobblia lunata* with improved K^+ selectivity, negligible photocurrent inactivation, and improved light sensitivity compared to both previously characterized KCRs. WiChR is well expressed in neurons and cardiac myocytes, where it showed reduced depolarization at negative membrane potentials and prolonged inhibition of APs with minimally invasive illumination protocols. Since WiChR is highly K^+ selective, well tolerated in different classes of excitable cells, and sensitive to holographic 2P excitation, we recommend WiChR as a versatile tool for multitarget single-cell inhibition in large cellular networks.

RESULTS

HcKCRs are K^+-selective channels with substantial Na^+ conductance

We expressed both HcKCRs in ND7/23 cells and compared photocurrents at different ionic conditions with those of ChRmine (Fig. 1B). In the presence of high intra- and extracellular K^+, large photocurrents confirmed efficient K^+ conductance for all three channels with even higher photocurrent densities for both HcKCRs than for ChRmine. Replacing high extracellular K^+ by Na^+ had no effect on the photocurrents of ChRmine, which conducts both cations equally well. For both HcKCRs, however, it caused a significant reduction of inward currents and a strong shift in the reversal potential confirming their pronounced preference for K^+ over Na^+ (Fig. 1, C to F). Furthermore, exchange of Na^+ for the larger cation NMG^+ abolished all remaining inward currents in HcKCRs and shifted the reversal potential in all three channels, indicating that in ChRmine, as well as in HcKCRs, Na^+ ions are conducted to a considerable extent. Moreover, at high external Na^+ and voltages close to E_{rev}, extended illumination led to a directional change of the HcKCR1 photocurrents and to a transition from a K^+ outward current to a Na^+ influx (Fig.1G), which reveals an increasing Na^+ conductance over time. The concomitant E_{rev} shifted by about 10 mV, which represents a decrease in the permeability ratio (P_{K+}/P_{Na+}) from 29 ± 4 to 18 ± 2 (fig. S1). In parallel, HcKCR1 photocurrents inactivate by 30 to 60% depending on the voltage and ionic conditions, and recover biphasically within seconds in the dark (fig. S2).

K^+ selectivity of HcKCRs relies on aromatic residues in the extracellular half pore

In the next set of experiments, we identified key amino acids relevant for efficient K^+ conductance and selectivity in HcKCR1. All known ChRs conduct ions along a sequence of preformed water-filled cavities between transmembrane helices 1, 2, 3, and 7 (*11*). For HcKCR1, we generated a refined three-dimensional (3D) model combining classical molecular dynamics (MD) simulations and pK_a (where K_a is the acid dissociation constant) predictions. The putative pore spans from the extracellular D87 in transmembrane helix 2 to the intracellular D116 in helix 3 (Fig. 2A). Aspartates D105 and D229 in the center of the pore constitute the counterion complex that stabilizes the protonated retinal Schiff base charge. The extracellular half pore is lined by a set of aromatic residues including Y81, F88, W210, Y222, and the unusual tryptophan W102 at a position most frequently occupied by arginine in other microbial rhodopsins.

Mutations of most pore-lining residues had little impact on the K^+ conductance and selectivity (figs. S3 and S4) or spectral properties (fig. S5). Accordingly, photocurrents of the central gate mutant C77A still resembled wild type (WT) like currents (Fig. 2, B and C). In contrast, mutations of S70, Y81, F88, and W210 that are located at various positions along the pore and partly in close contact with the pore aspartates caused a strong reduction of outward currents (S70A, Y81F, and W210A) and impaired K^+ selection, as indicated by the diminished ΔE_{rev} (S70A, F88T, and W210A). A nearly complete loss of K^+ selectivity was observed for the outer pore mutant N99L and for substitutions of W102 and Y222 by nonaromatic residues such as W102Q and Y222A. For all three mutants, inward currents were large at high extracellular Na^+ or K^+ (Fig. 2C), with little reversal potential shift between the two conditions (Fig. 2D), very similar to the nonselective cation channel ChRmine (Fig. 1, C and F). K^+ selectivity was also compromised in D87 and D116 mutants but came with a near-complete loss of stationary photocurrents (Fig. 2E). Mutations of the counterion complex also showed reduced photocurrent amplitudes but largely preserved K^+ selectivity. In conclusion, all four aspartates of the pore and their putative interaction partners S70, Y81, and F88 are essential for channel gating and pore formation in KCRs, whereas W102, Y222, and N99 constitute essential elements of a unique hydrophobic K^+ selectivity filter. On the basis of our mutational analysis, we identified the quintet D87, N99, W102, D116, and Y222 as KCR signature motif that requires functional support by the nearby residues S70, F88, D105, and W210 (Fig. 3A).

Identification of further candidate KCRs

A systematic search revealed that KCRs from *H. catenoides* [HcKCR1 and HcKCR2 (*17*)] as well as the nonselective cation channel from the same organism [*HcCCR* (*21*)] are part of a bigger clade that unites ChRs from a small set of stramenopile protists and related metatranscriptomic sequences (Fig. 3B and figs. S6 and S7A). The four non-hyphochytridiomycete stramenopiles that were found to possess ChRs from this group are heterotrophic flagellates from the Opalozoa clade: placidids *W. lunata* and Placidida sp. Caron Lab Isolate and anoecids *Cafeteria burkhardae* and *Bilabrum* sp. (the latter identified using molecular markers). Together with cryptophyte CCRs (including ChRmine) and a so far not described clade of uncharacterized ChRs from colpodellid alveolates, these proteins form a well-supported monophylum (Fig. 3B and fig.

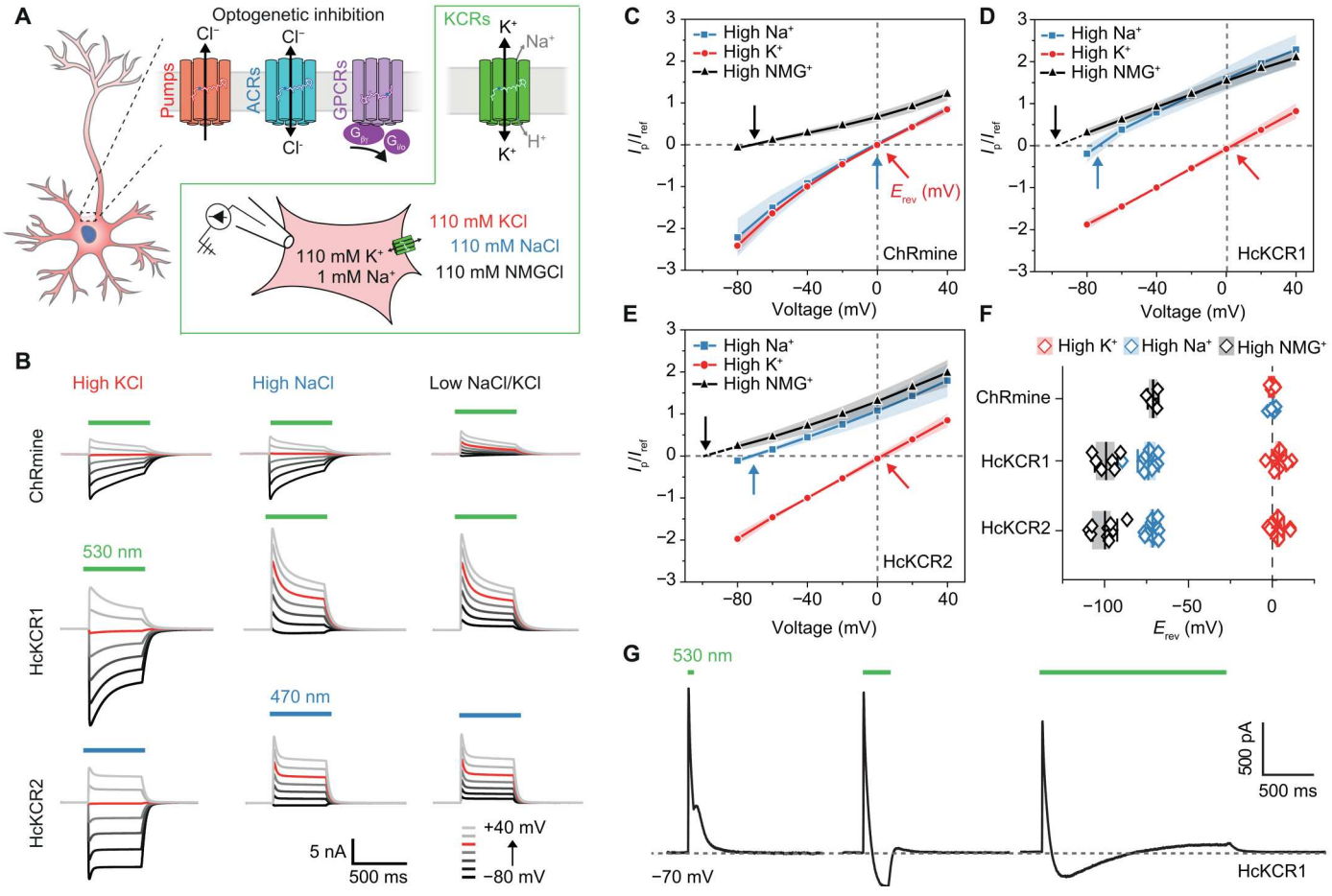

Fig. 1. K^+ selectivity of HcKCRs. (**A**) Established optogenetic inhibitory tools, including light-driven ion pumps (red), anion selective channelrhodopsins, ACRs (blue), and $G_{i/o}$-coupled opsins (purple). Potassium-selective ChRs, KCRs (green) and used measuring conditions for (B) to (G) are seen inside the green box. (**B**) Photocurrents of ChRmine, HcKCR1, and HcKCR2 at 110 mM K_e^+, Na_e^+, or NMG_e^+ and 110 mM K_i^+ gluconate with $pH_{e/i}$ 7.2. (**C** to **E**) *I*(*E*) relations of the normalized peak photocurrent amplitudes I_p/I_0 (mean ± SD and *n* = 7/7/4 for ChRmine, *n* = 10/10/6 for HcKCR1, and *n* = 13/13/9 for HcKCR2). (**F**) E_{rev} values for (C) to (E) that were linearly extra- or interpolated close to the reversal potential. (**G**) Photocurrents of HcKCR1 at −70 mV and high Na_e^+ upon 50-ms, 250-ms, and 2-s illumination.

S6A). Most stramenopile CCRs share the functionally important DTD motif of bacteriorhodopsin (D85, T89, and D96) in transmembrane helix 3 with cryptophyte CCRs. The minor variations DSD, DSE, ETD, and DLD found in the other Stramenopiles preserve both of the carboxylates, whereas in related colpodellid proteins only the second aspartate is conserved (GGD motif) (fig. S6B). Clustering of the stramenopile CCRs and cryptophyte CCRs indicates that cation conductivity is ancestral in this lineage.

Among the collected stramenopile ChRs from this clade, two proteins, WlChR1 from *W. lunata* and B1ChR2 from *Bilabrum* sp., contained a nearly complete KCR signature motif with only one conservative substitution at the position of Y222 for phenylalanine—a substitution that preserved K^+ selectivity in HcKCR1 in our mutational analysis (fig. S4).

Electrophysiological characterization of WlChR1 (WiChR) in cultured cells

Expressed in ND7/23 cells, WlChR1 showed excellent membrane targeting (Fig. 3C and fig. S9) and large photocurrents with almost no inactivation during prolonged illumination (Fig. 3D). In contrast, B1ChR2 aggregated substantially in intracellular compartments and produced photocurrents with rapid inactivation and strong inward rectification. Photocurrent recordings at different K_e^+ concentrations confirmed a high K^+ selectivity for both channels. Notably, WlChR1 and B1ChR2 even showed a complete loss of inward-directed currents upon exchange of extracellular K^+ to Na^+ (Fig. 3, E and F). The corresponding larger ΔE_{rev} for WlChR1 in comparison to HcKCR1 (Fig. 3G) is interpreted on the basis of the Goldmann-Hodgkin-Katz voltage equation as a remarkable increase in relative K^+ conductance from $P_{K+}/P_{Na+} = 18 \pm 2$ for the late photocurrent of HcKCR1 (fig. S1) to $P_{K+}/P_{Na+} = 80 \pm 40$ for stationary photocurrents of WlChR1. Improved K^+ selectivity is accompanied by enlarged stationary photocurrents (Fig. 3H)—explained by the good expression and reduced photocurrent inactivation—and slow channel closure (Fig. 3I) that together result in an improved operational light sensitivity (Fig. 3J). The blue-shifted action spectrum compared to HcKCR1 favors a combination with red-absorbing actuators and sensors and largely overlaps with HcKCR2 (Fig. 3K). Considering WlChR1 as a highly promising tool for optogenetic inhibition, we term it WiChR for "*Wobblia* inhibitory channelrhodopsin".

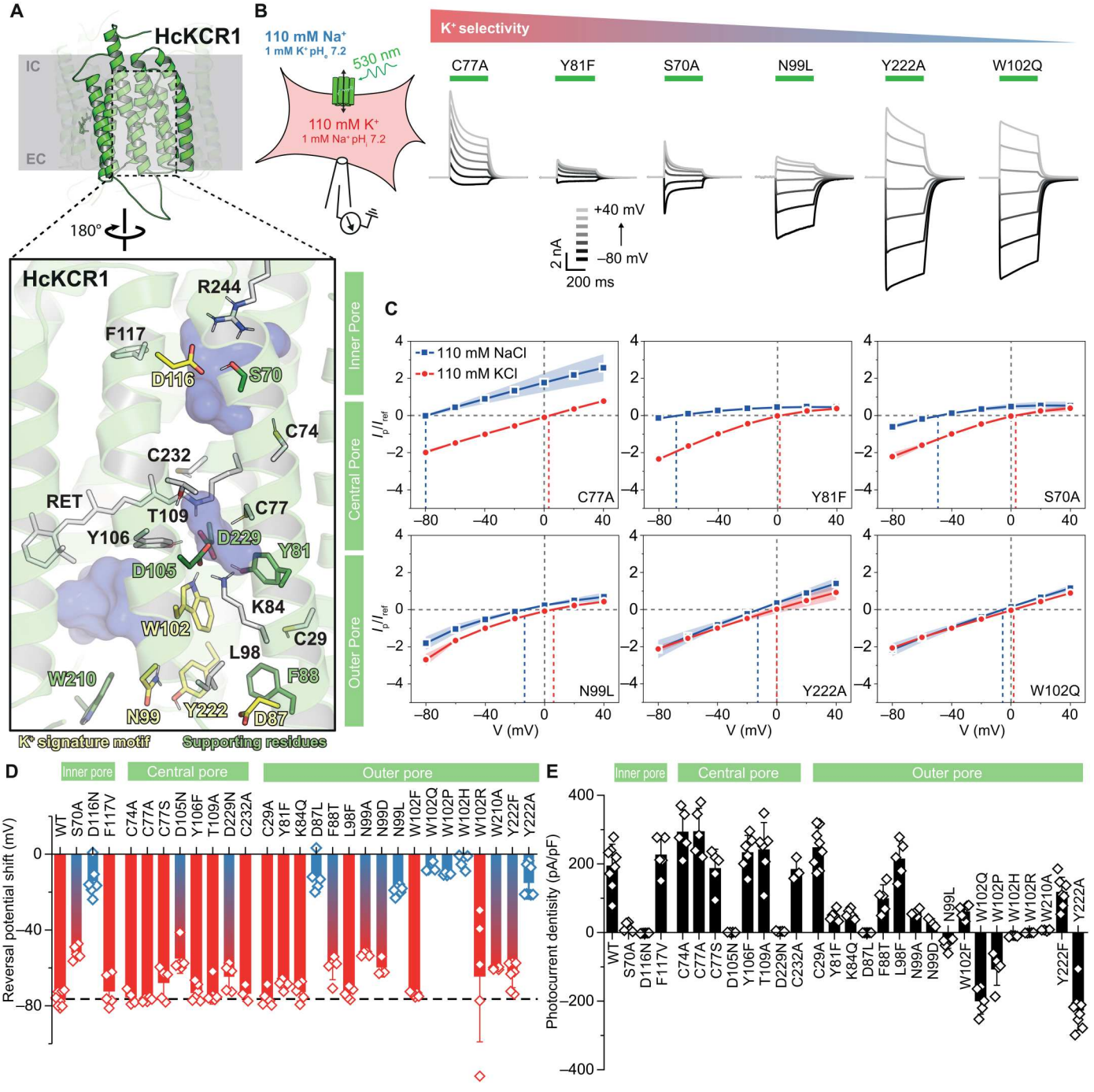

Fig. 2. Molecular determinants of K⁺ conductance in KCRs. (**A**) Equilibrated AlphaFold2 3D model of HcKCR1 with important residues lining the putative pore highlighted in yellow (K^+ signature motif) and green (supporting residues). (**B**) Representative photocurrents of pore lining HcKCR1 mutants at 110 mM Na_e^+ and 110 mM K_i^+, with C77A resembling the WT. (**C**) I(E) relations of the normalized peak photocurrent amplitudes of selected mutants. (**D**) ΔE_{rev} for extracellular buffer exchange from high K_e^+ to Na_e^+. (**E**) Photocurrent density at −40 mV and 110 mM Na_e^+. All plots show mean ± SD (n = 3 to 8).

Molecular determinants of improved K⁺ selectivity in WiChR

The improved K^+ selectivity of WiChR compared to HcKCR1 was expected to be caused by two side-chain substitutions in the extracellular part of the pore, which are F240 within the K^+ selectivity filter itself (Y222 in HcKCR1) and D47 in the direct vicinity of the important helix-3 tryptophan W120 (C29 in HcKCR1). Both are highlighted in the thermally equilibrated AlphaFold2 model in Fig. 4A. Mutation of both residues impaired K^+ selection in WiChR with a remarkably reduced reversal potential shift upon K^+ to Na^+ replacement for WiChR D47C in comparison to the WT channel. Mutation of the same residues in HcKCR1 also slightly reduced K^+

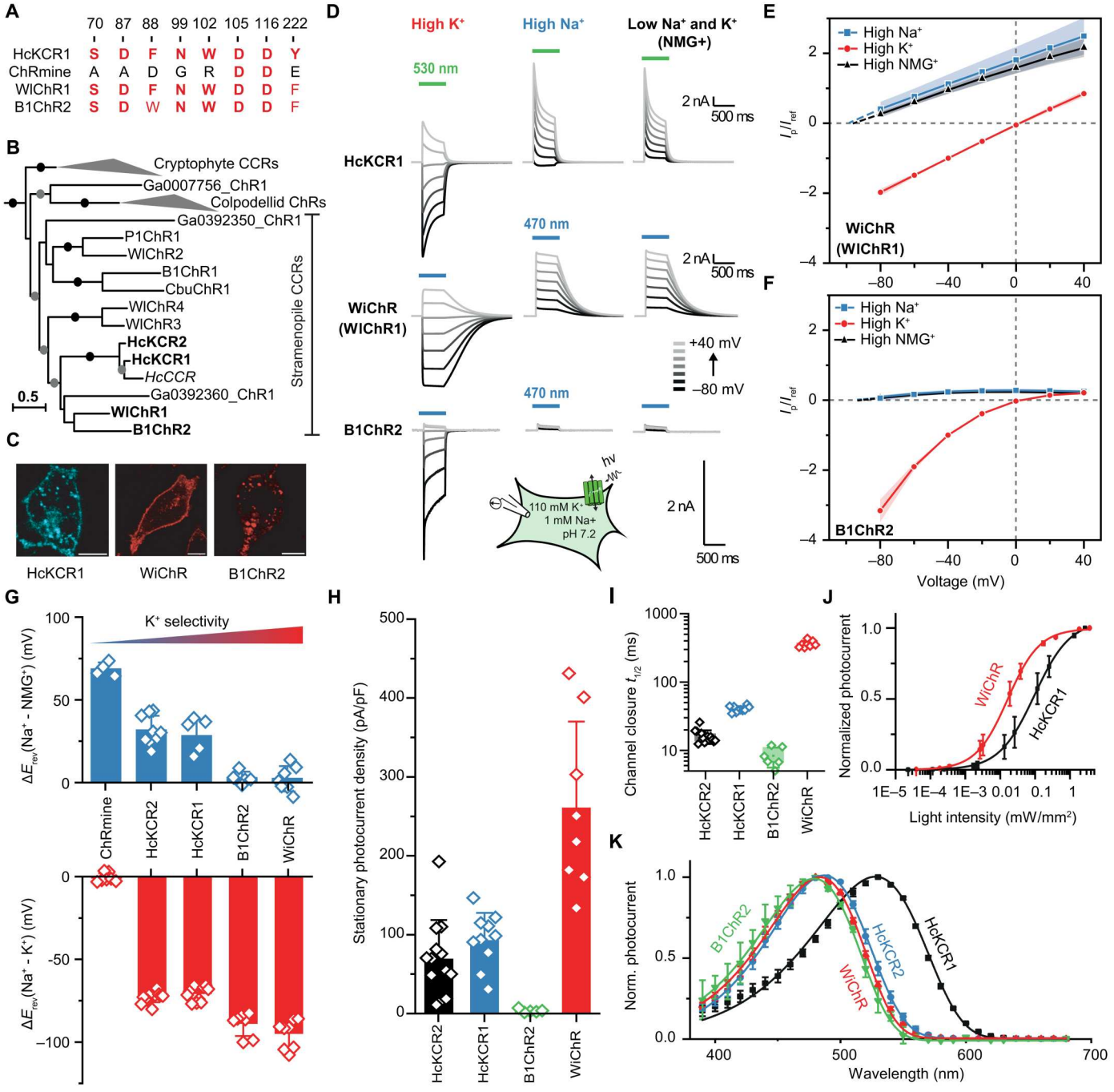

Fig. 3. Identification and characterization of WiChR. (**A**) The eight–amino acid motif of the K^+ selectivity filter in red (see also fig. S6A and the complete alignment in fig. S8 and data S4). (**B**) Phylogenetic relationships among the stramenopile CCRs (see the complete phylogenetic tree of the ChR family in fig. S6A and data S2). Dots represent ultrafast bootstrap support values: ≥80 (gray) and ≥95 (black). (**C**) Cellular distribution of the fluorescence-tagged KCRs. (**D**) Representative photocurrents of HcKCR1, WiChR, and B1ChR2 at high K_e^+, Na_e^+, or NMG_e^+ and intracellular 110 mM K_i^+ gluconate at $pH_{e/i}$ 7.2. (**E** and **F**) *I*(*E*) relations of the peak photocurrent amplitudes of WiChR/WiChR1 (n = 8/8/7) and B1ChR2 (n = 7/7/5). (**G**) ΔE_{rev} of stationary photocurrents (after 500-ms illumination) for extracellular buffer exchange from high K_e^+ to Na_e^+ (bottom) and high Na_e^+ to NMG_e^+. (top). (**H**) Stationary photocurrent densities with high Na_e^+ and −40 mV. (**I**) Photocurrent closure after 500-ms recordings. (**J**) Light titration of the WiChR (n = 5) and HcKCR1 (n = 5) peak photocurrents. (**K**) Action spectra of peak photocurrents (n = 6 for all four channels). All plots show mean ± SD.

selectivity for HcKCR1 Y222F, as discussed before (Fig. 2E), but it further improves K^+ selection for HcKCR1 C29D (Fig. 4E), which we identified as a further essential modulator of the ChR K^+ selectivity filter.

2P-holographic inhibition of neurons in organotypic slices

To explore the potential of WiChR for neuronal application, we expressed HcKCR1 and WiChR in organotypic slices from the mouse hippocampus and compared their inhibitory performance using

holographic 2P patterned stimulation with a low repetition rate (500 kHz) pulsed laser at 1030 nm (Fig. 5A). Both KCRs expressed well (Fig. 5B) and showed no signs of toxicity (fig. S12). We injected depolarizing square currents (1 s) to induce AP firing and illuminated in the middle of the current injection. Both HcKCR1 and WiChR completely inhibited spiking at current injections well above the respective rheobase of the neuron (Fig. 5B). However, while for HcKCR1 continuous illumination was needed, for WiChR a single 5-ms pulse was sufficient to achieve a complete cessation of firing for the entire 500 ms (Fig. 5B and C). Since extended periods of inhibition are often needed during in vivo applications, pulsed illumination reduces the local heating in the tissue compared to continuous illumination. Hence, we compared inhibition with continuous illumination to the application of 5-ms pulses at 10, 5, and 2 Hz and found that in slices WiChR achieves a complete cessation of AP firing down to a frequency of 2 Hz, while HcKCR1 needs continuous illumination for a comparable degree of inhibition (fig. S13, A and B).

Next, we simulated the local temperature rise (*22*) for the holographic spot (12 μm diameter, 31 μW/μm^2) and compared continuous to pulsed illumination. We found that heat accumulates with continuous illumination, while the pulsed protocol at 10, 5, or 2 Hz allows for dissipation of the heat before the next pulse (fig. S13C). While for one holographic spot, the local temperature rise of ~0.2 K (continuous) and ~0.1 K (pulsed) is still far below the reported thermal damage threshold of ~1 K, most applications will demand inhibition of more than one neuron in a given region. Here, our simulations show that with a 5-ms pulsed illumination, peak heating stays below 1 K, and no heat is accumulated over time, even when placing up to 40 holographic spots within a small 100 μm × 100 μm area. On the contrary, for continuous illumination, heat is accumulated and increases linearly with the number of spots, reaching almost 4K for the same 40 spots (fig. S13D).

When we injected hyperpolarizing current steps to have more negative membrane potentials, we found that illumination caused depolarization instead of further hyperpolarization for both HcKCR1 and WiChR (Fig. 5D), which can be explained by their residual Na^+ conductance. However, reversion from hyperpolarization to depolarization occurred at a significantly more negative membrane potential of −92 ± 2 mV for WiChR than for HcKCR1 (−80 ± 4 mV) (Fig. 5, E and F), confirming the higher K^+ selectivity of WiChR.

To compare the operational light sensitivity of HcKCR1 and WiChR at 1030 nm, we used a somatic ramp current injection to induce APs and increase light intensities during the current injection to characterize the efficiency of inhibition (Fig. 5G, left). For both KCRs, increasing light intensities delayed the first AP on the

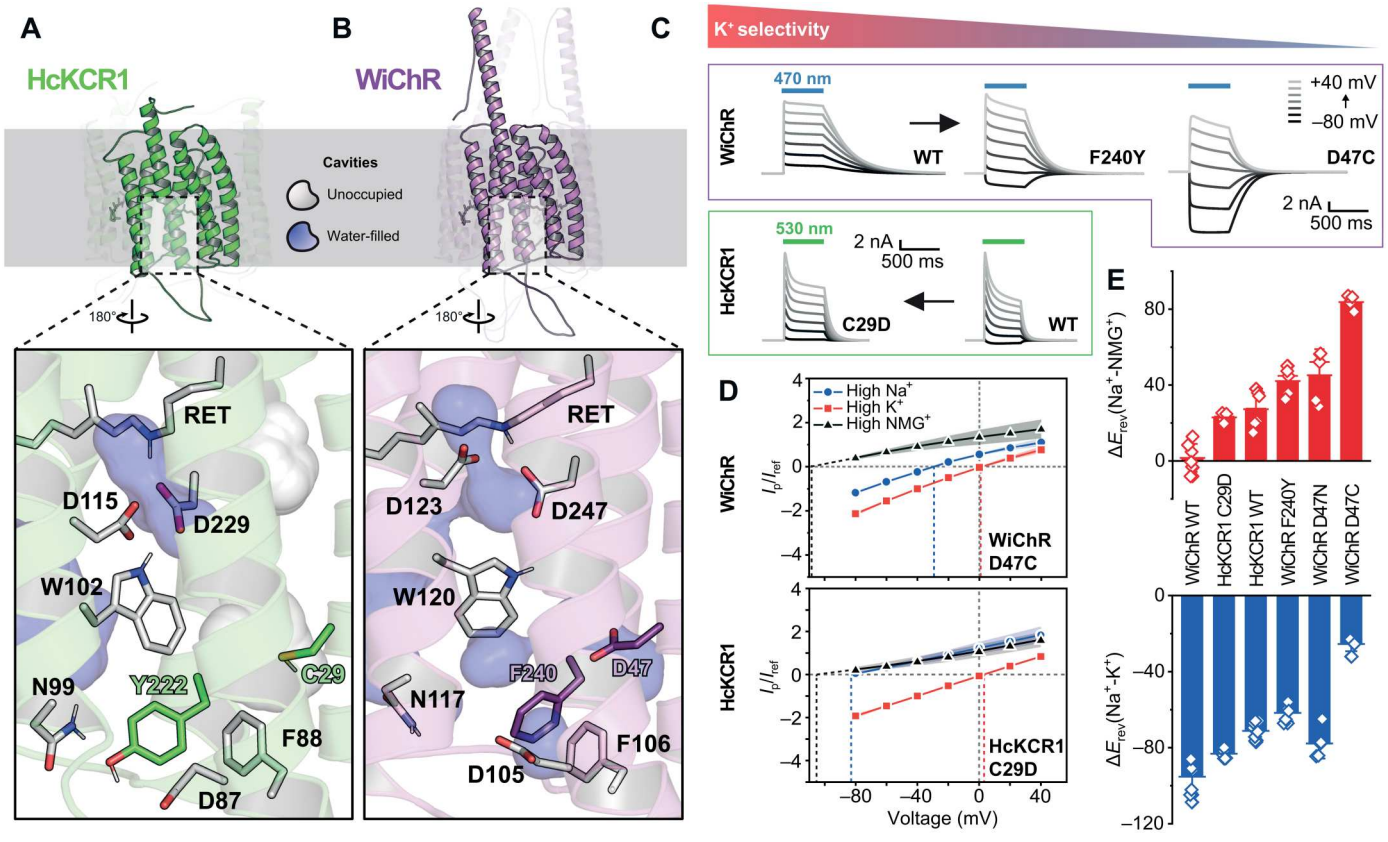

Fig. 4. K^+ selectivity of WiChR. (**A** and **B**) 3D models of HcKCR1 and WiChR with residues that are important for K^+ conductance highlighted in green and magenta. (**C**) Representative photocurrents of K^+ selectivity determinants in WiChR and HcKCR1 at 110 mM Na^+_e and 110 mM K^+_i gluconate. (**D**) $I(E)$ relations of the normalized peak photocurrent amplitudes of WiChR D47C (n = 5/5/5) and HcKCR1 C29D (n = 6/5/4) (mean ± SD). (**E**) ΔE_{rev} (Na^+_e − NMG^+_e) (top) and ΔE_{rev} (Na^+_e − K^+_e) (bottom) of stationary photocurrents (after 500-ms illumination) (mean ± SD).

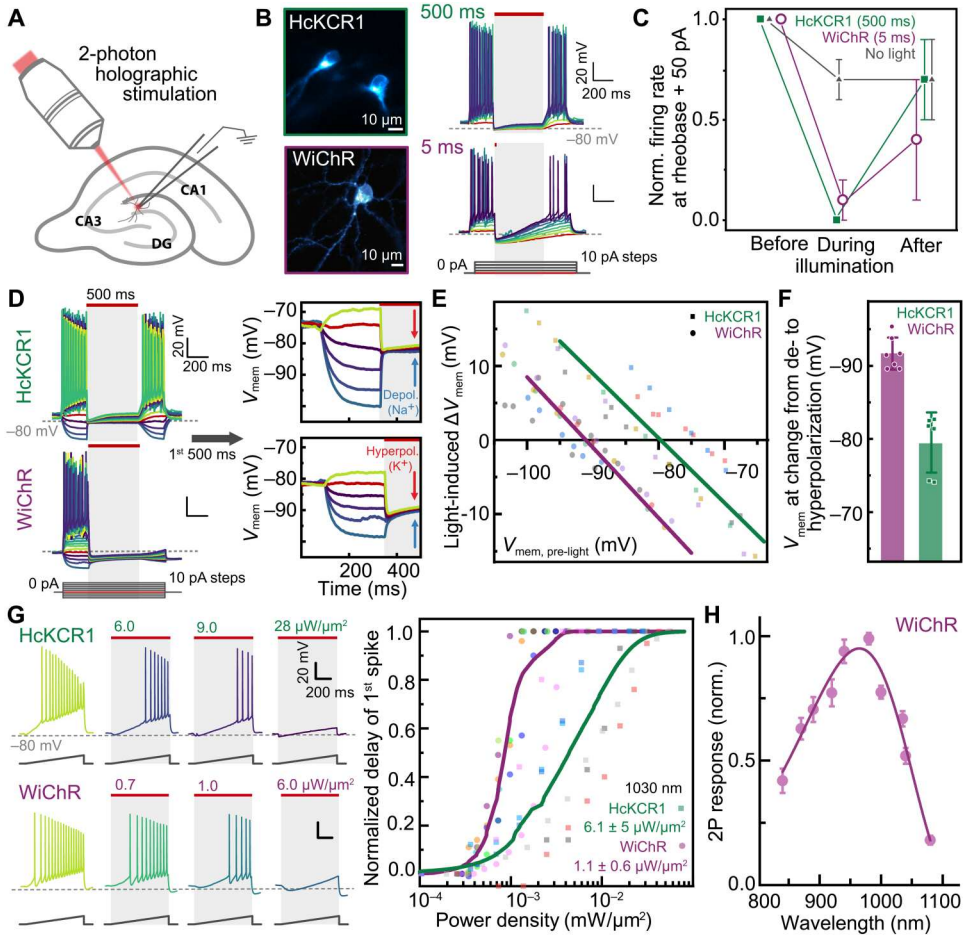

Fig. 5. Neuronal inhibition with 2P holographic stimulation of WiChR in organotypic hippocampal slices. (**A**) Whole-cell patch-clamp recordings of HcKCR1- and WiChR-expressing neurons with 2P holographic illumination (1030 nm); LJP corrected for all recordings. (**B**) 1P wide-field epifluorescence images of HcKCR1- and WiChR-expressing neurons and recordings of square depolarizing current injections (1 s) with a 500-ms period of photoinhibition within this time; continuous illumination for HcKCR1 and 5 ms for WiChR (29 µW/µm^2). (**C**) Normalized firing rate 50 pA above rheobase for HcKCR1, WiChR [as in (B)], and without light: mean ± SD, $n = 6$ to 8 each. (**D**) Current-clamp recordings like in (A) with hyperpolarizing current injections showing light-induced depolarization (right) for HcKCR1 and WiChR at negative membrane potentials. (**E**) Light-induced potential change at different membrane potentials showing both hyperpolarization and depolarization upon illumination; points represent individual recordings and lines are the average. (**F**) Extrapolation of membrane potential where illumination induces depolarization instead of hyperpolarization (mean ± SD). (**G**) Depolarizing somatic ramp current injections with continuous illumination of rising power densities during ramp and normalized light-induced delay of first spike on the ramp relative to the dark; 0, no delay; 1, no AP during ramp. Points represent individual recordings, and lines are the average of the logistic fits; $n = 6$, $n = 7$; median effective concentration (EC_{50}) values, mean ± SD. (**H**) 2P response of WiChR for varying wavelengths. Measured in ND7/23 cells with a tunable high repetition rate laser. 2P response as normalized slope of the photocurrent rise within 3 ms (linear fit); $n = 5$, mean ± SD.

ramp compared to darkness, but half-maximal inhibition was observed at six times lower power densities for WiChR than for HcKCR1 (Fig. 5G, right). For HcKCR1, complete suppression of spiking on the ramp was achieved at 43 µW/µm^2, while for WiChR, this was reached for all patched neurons already at 4.4 µW/µm^2. Last, for 2P dual-color application using WiChR in combination with other optical probes, we measured the 2P action spectrum between 840 and 1080 nm (Fig. 5H; for details, see Materials and Methods) and found the maximal sensitivity between 940 and 980 nm excitation.

In vivo 2P-holographic inhibition with WiChR

After characterizing neuronal inhibition through WiChR in vitro, we sought to demonstrate the effectiveness of WiChR-mediated inhibition in vivo. On the basis of the plasmid used for slice electroporation, we generated a WiChR-mScarlet–encoding adeno-associated virus (AAV), which we injected into the primary visual cortex of mice. Five weeks after injection, we found efficient opsin expression (Fig. 6A) and we explored the effectiveness of inhibition with WiChR in vivo by whole-cell patch-clamp recordings in anesthetized mice. We injected square currents above the respective rheobase of the neuron to evoke APs and applied the pulsed illumination protocol in the middle of the current injection (Fig. 6B, left). We found a significant reduction of the AP frequency (two mice, $n = 3$ cells) during the 10-Hz train of 5-ms pulses, verifying the applicability of WiChR and the pulsed illumination protocol in vivo. In addition, we found that an increase in the illumination frequency could increase the effectiveness of inhibition (fig. S14B) in accordance with our in vitro results from slices (fig. S13).

WiChR-mediated inhibition of the electromechanical activity of atrial CMs

For a test of efficacy in non-neuronal excitable cells, we tested the ability of WiChR to inhibit spontaneous activity of human induced pluripotent stem cell (hiPSC)–derived atrial CMs (aCMs). aCMs were transiently transfected with plasmids encoding WiChR-mScarlet, leading to sparse but robust channel expression in the sarcolemma, as visualized by mScarlet fluorescence (Fig. 7A). In WiChR-expressing cultures, blue light applied for 10 s caused fully reversible inhibition of spontaneous contractions (Fig. 7B and movie S1). In 10 of 11 recordings, WiChR-elicited currents (fig. S15A) were sufficient to fully inhibit APs in syncytia of electrically coupled aCM (Fig. 7, C and D). Maximum diastolic potentials and end-diastolic potentials (so-called take-off potentials) were not different between WiChR-expressing and non-transfected cultures. Initial illumination induced a small hyperpolarization of membrane potential (inset IIA in Fig. 7C). During prolonged light application, the membrane potential slightly depolarized compared to the maximal diastolic potentials before and after light application (P = 0.013) but was similar to end diastolic potentials (Fig. 7, E and F). Membrane potential and all AP parameters (AP duration, frequency, and upstroke velocity) were restored within 10 APs after illumination (fig. S15, B to D).

DISCUSSION

KCRs constitute a new group of light-gated ion channels. In this study, we investigated their molecular mechanism and identified the amino acid motif that is required for their high K^+ selectivity. Exploiting that knowledge, we uncovered two additional KCRs with significantly improved K^+ selectivity and, in the case of WiChR, with excellent inhibitory performance in neurons and CMs.

Our results show that the K^+ selectivity of KCRs relies on an unusual pair of aromatic residues in helices 3 and 7 that occlude the extracellular pore in the dark and constitute the K^+ selectivity filter in the open channel (W102 and Y222 in HcKCR1, highlighted in Fig. 8A and fig. S10, which is unique among rhodopsins. In addition, six further residues are required for efficient K^+ conductance. Among them are three pore-lining carboxylates (D87, D105, and D116 in HcKCR1) found at similar positions in ChRmine (*20*), which are expected to be generally involved in channel gating, similarly, as earlier discussed, for the related GtCCR2 (*23*). Last, three side chains of putative secondary importance (S70, F88, and L99 in HcKCR1) ensure conformational integrity of the pore and orientation and hydrophobicity of the K^+ selectivity filter.

The identified K^+ filter contrasts the conserved mechanism of ion selectivity in conventional highly symmetric tetrameric K^+ channels, like KcsA or K_v, where K^+ ions are conducted along the tetramer interface and are tightly coordinated by backbone carbonyl

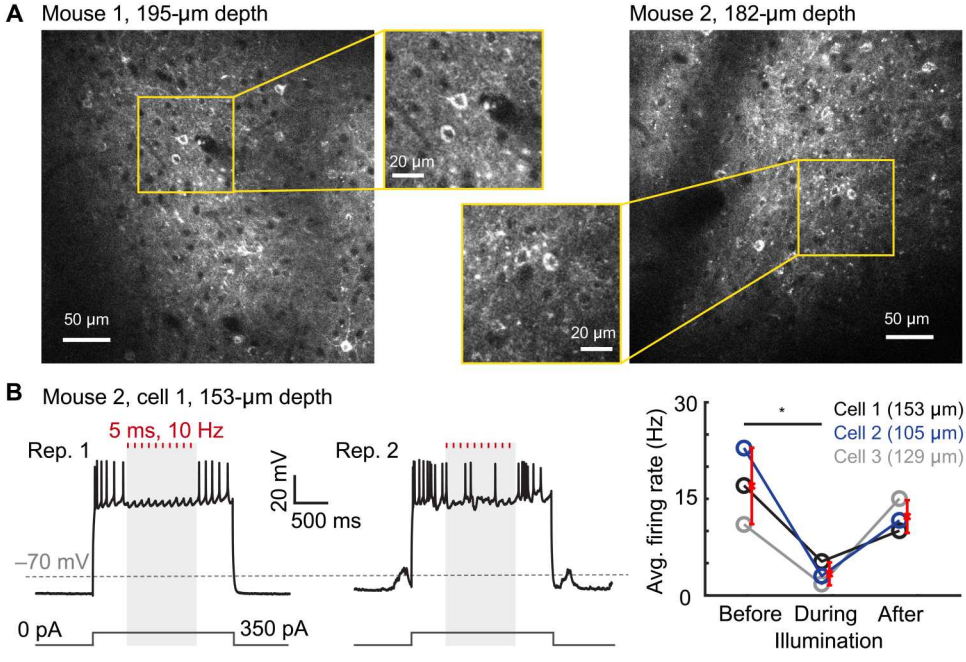

Fig. 6. Neuronal inhibition with 2P holographic stimulation of WiChR in mouse visual cortex. (**A**) 2P images of WiChR-mScarlet expression in layer 2/3, 195 µm and 182 deep µm, of visual cortex in anesthetized mice; mouse 1, 5 weeks and mouse 2, 11 weeks after viral injection. Zoom-in views showing neurons expressing WiChR-mScarlet. The images were acquired by 2P scanning at a frame rate of 1 Hz at 980 nm in mouse 1 and 960 nm in mouse 2. (**B**) Left: Sample traces from a whole-cell recording of a WiChR-expressing neuron in layer 2/3 of visual cortex in a lightly anesthetized mouse, demonstrating suppression of electrically induced APs by 10-Hz trains (5 ms) of temporally focused 2P holographic illumination targeting the patched cell soma (spot diameter 12 µm, 7 to 8 mW). Traces of two repetitions are shown, and the photostimulation is indicated in red; membrane potential was corrected for an LJP of +11.9 mV. Right: Average firing rates across repetitions before, during, and after illumination calculated for three cells from two different mice; mean ± SD across cells is plotted in red. For traces and individual firing rates of each cell, see fig. S14A. The average firing rates were significantly modulated in the three conditions [one-way analysis of variance (ANOVA), P = 0.013]. Significant difference in average firing rates was denoted as asterisk (multiple comparisons between conditions).

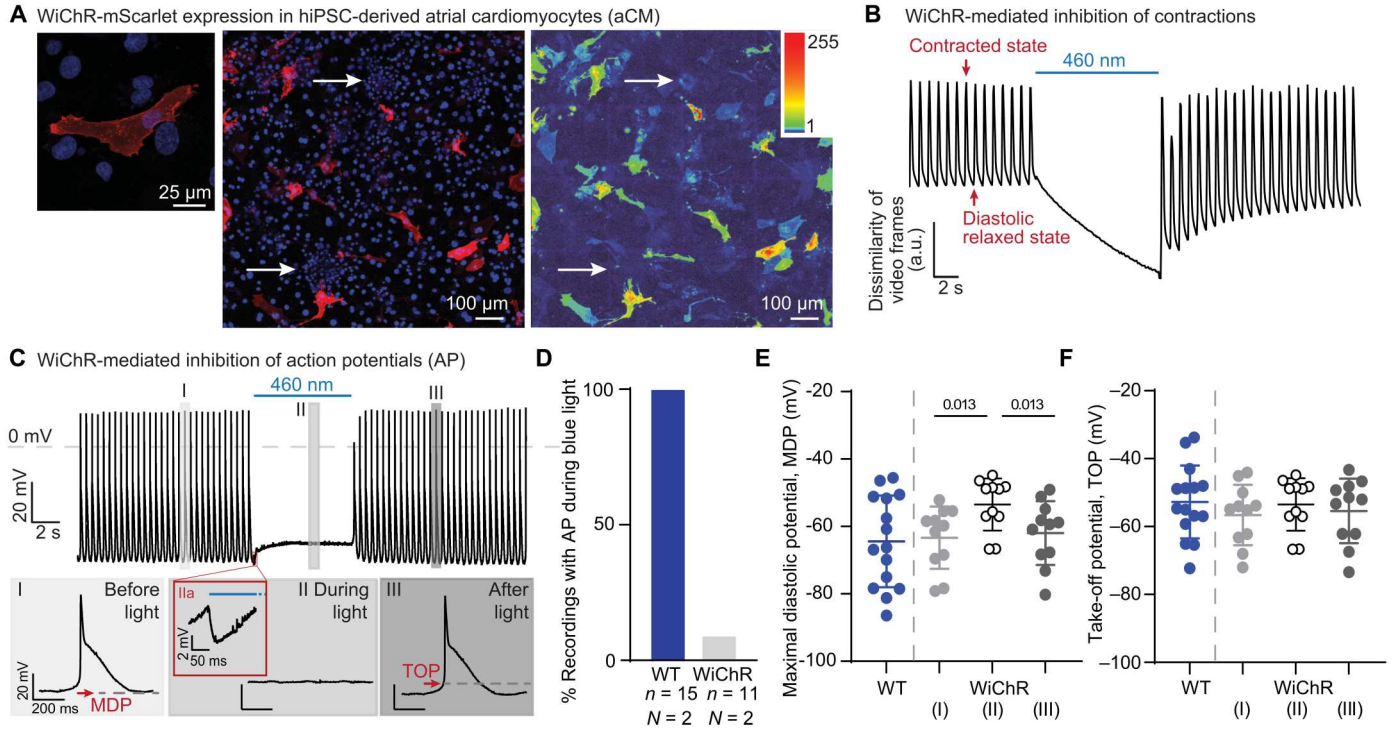

Fig. 7. WiChR is a potent tool for silencing the activity of hiPSC-derived aCMs. (**A**) Confocal images showing WiChR-mScarlet expression (in red) and DAPI staining of nuclei (in blue). White arrows indicate cell clusters from which cells were chosen for sharp electrode recordings (in a blinded way in respect to mScarlet fluorescence). (**B**) Analysis of representative video showing WiChR-mediated inhibition of contractions. WiChR-expressing aCM cultures were imaged by wide-field transmission microscopy. Graph shows dissimilarity score based on pixel-wise comparison of intensities (see Materials and Methods for details). a.u., arbitrary units. (**C**) Sharp electrode recording showing reversible inhibition of AP during blue light application. Insets in bottom row show AP before light (phase I), absence of AP during illumination (phase II, including initial phase of illumination IIa), and APs after light (phase III). (**D**) Quantification of recordings with AP during light application comparing non-transfected control cultures (WT) to cultures expressing WiChR. (**E** and **F**) Comparison of maximum diastolic potential (MDP) and take-off potential (TOP) in control cultures to WiChR-expressing cultures in phases I (average of 10 AP before light application) and III (average of 11th to 20th AP after light), respectively (closed circles). For phase II (during light application), the average membrane potential between 4.5 and 5.5 s of illumination is plotted (open circles). Mann-Whitney test was used for group-wise statistical analyses.

oxygens of the selectivity filter (*24*). However, for KCRs, our equilibrated structural models and the results of our mutational analysis predict a trimeric assembly with an inter-subunit cavity most likely filled with lipids similar to ChRmine (*19*) and an ion permeation pathway going through the individual KCR protomers themselves. We propose that the passage of K^+ ions requires dehydration to pass

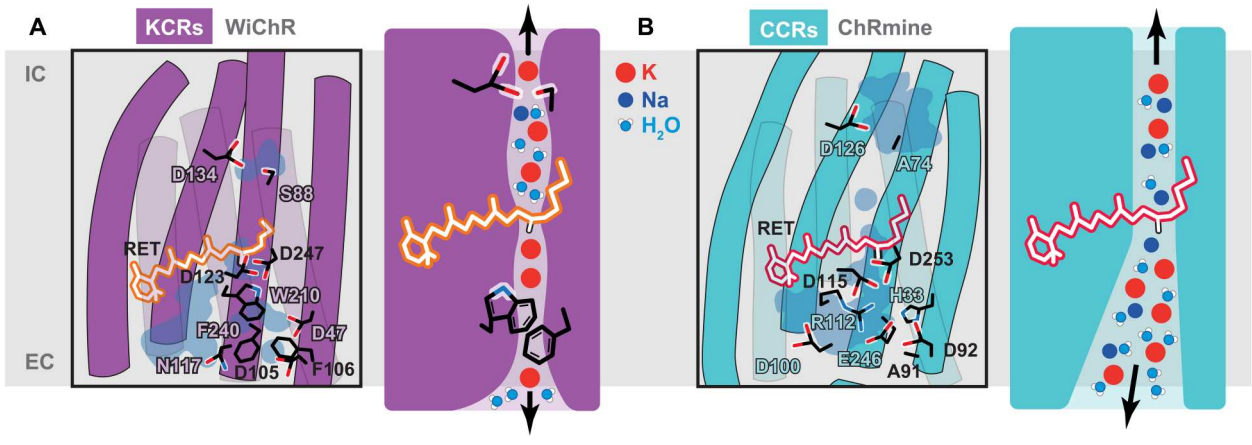

Fig. 8. Selectivity filter of KCRs compared to related cryptophyte CCRs. (**A**) Structural model of the WiChR dark state (left) and a simplified open-state representation with putative pore constrictions that are important for K^+ selectivity at the intracellular (IC) and the extracellular (EC) side of the protein. (**B**) Cartoon model of the ChRmine dark state and a simplified representation of its assumed open state configuration.

the hydrophobic and aromatic side chains of the K^+ selectivity filter where passage of Na^+—with higher dehydration energy and more localized charge—is blocked. In the related ChRmine, the wider and presumably water-filled access funnel could allow permeation of partly hydrated K^+ and Na^+ (Fig. 8). A similar non-canonical mechanism for K^+ selectivity was recently described for the lysosomal K^+ channel TMEM175, which also features a hydrophobic restriction in the center of the pore, as required for K^+ conductance, and which also showed important differences in K^+ selectivity for different channel subtypes, ranging from P_{K+}/P_{Na+} of 2 in bacteria to P_{K+}/P_{Na+} of 35 in humans (*25*). Accordingly, P_{K+}/P_{Na+} also varied significantly for different KCRs despite the overall conserved signature motif. In these channels, minor differences in the pore, such as WiChR D47 at the position of HcKCR1 C29, seem to affect the orientation and interaction of amino acids in the filter and the pore explaining the differences in K^+ selectivity (fig. S10, B and C).

With the ability to control K^+ flux in optogenetic experiments, KCRs can be applied for inhibition of so far inaccessible systems of excitable cells. These include cellular and subcellular compartments with elevated intracellular chloride concentrations such as synaptic terminals or cardiac muscle cells, where activation of ACRs can have depolarizing effects leading to cellular excitation (*7*, *8*). Here, we demonstrated robust and reversible inhibition of contractions and APs in hiPSC-derived aCM cultures expressing the identified WiChR channel. In contrast to previously used ACRs, inhibition was achieved without major changes in membrane potential.

While in neurons effective inhibition may also be achieved with HcKCR1, the discovered WiChR outperforms HcKCRs in several applications based on three properties. First, the K^+ selectivity over Na^+ is more than three times higher for WiChR compared to HcKCR1, which allows effective inhibition of neurons over a broader range of resting potentials and less dependent on the Na^+ gradient. Second, the high operational light sensitivity of WiChR allowed inhibition at an order of magnitude lower photon exposure compared to HcKCR1 with both 1P and 2P illumination. Especially the high efficiency of activation with holographic 2P illumination will facilitate light delivery for in vivo experiments and increase the accessible depth of successful optical inhibition while single-cell resolution is maintained. In addition, it allows for the distribution of available laser power over a larger number of target cells and, hence, simultaneous inhibition of a larger group of cells. Third, the longer open-state lifetime of WiChR is fundamental to the pulsed illumination protocol, the applicability of which we extensively investigated here and verified for in vivo studies. Continuous illumination, as necessary for HcKCRs, will cause a significant temperature rise in the tissue, especially considering the extended time frames and the number of cells to be inhibited that can be needed for behavior experiments. On the contrary, the pulsed illumination can be applied for long duration and for many target cells without any heat accumulation in the tissue presenting a tremendous advantage for in vivo application.

For future in vivo experiments, it should be considered that WiChR′s high light sensitivity, slow kinetics, and maximal sensitivity between 940 and 980 nm (Fig. 5H) render its combination with optical probes of similar spectral sensitivity, such as GCaMP (*26*), rather challenging and demand a careful calibration of the imaging conditions to avoid cross-activation. Instead, a combination with red-shifted dyes, e.g., RCaMP (*27*) or R-GECO (*28*), 2P excited at wavelengths beyond 1100 nm, is a possible alternative and should be explored for all-optical use in the future. Besides that, WiChR is well suited for in vivo experiments with a non-optical readout.

In conclusion, we recommend WiChR as the tool of choice for targeted inhibition of excitable cells across different organs. Excellent performance under 1P and 2P illumination shows major promise for reliable and reversible inhibition of large networks of electrically coupled cells and simultaneous silencing of tens to hundreds of neurons in intact tissue using low light intensities and short illumination times and with minimal photodamage.

MATERIALS AND METHODS

Search for ChR genes

ChRs from the stramenopile CCR subfamily: CbuChR1 [National Center for Biotechnology Information (NCBI) GenBank KAA0157615.1, NCBI genome assembly GCA_008330645.1] from *C. burkhardae* BVI (formerly, *Cafeteria roenbergensis* BVI), P1ChR1 (MMETSP1104_DN12643_c6_g1_i1, MMETSP assembly MMETSP1104) from Placidida sp. Caron Lab Isolate (formerly, "*Cafeteria*" sp.), and partial sequences of B1ChR1 and B1ChR2 from *Bilabrum* sp. (found as contamination in various algal transcriptome assemblies, in particular *Chroodactylon ornatum*; see text S1) were previously reported in (*4*). ChRs of *W. lunata* NIES-1015 (WlChR1-4) were obtained by assembling the raw data available from NCBI SRA (Short Read Archive) [SRA run DRR049555, (*29*)] with Trinity v. 2.13.2 (*30*). Search for ChR genes in these and other assemblies was performed by querying protein sequences using microbial rhodopsin HMM profiles (Profile Hidden Markov Models) (https://github.com/BejaLab/RhodopsinProfiles) with hmmsearch from HMMER v. 3.3.2 (*31*). ChR sequences were obtained by searching against a curated database of microbial rhodopsins using blastp from blast+ v. 2.11.0+ (*32*). The complete list of searched stramenopile assemblies is provided in data S1. De novo assemblies when necessary were obtained using Trinity for transcriptomes or spades v. 3.14.1 (*33*) for genomes and single amplified genomes (SAGs). Genes were predicted with TransDecoder v. 5.5.0 for transcriptome assemblies and GeneMarkS v. 4.32 for genome and SAG assemblies. Additional sequences related to stramenopile CCRs were obtained from JGI freshwater and marine metatranscriptomes using blast with stramenopile CCRs as queries. Only publicly available complete sequences from JGI were used in the analyses. A curated catalog of ChRs including sequences reported here is maintained in (*34*).

Phylogenetic analysis

Phylogeny of the stramenopile CCRs, related clades, and a reference set of ChRs from other families was obtained as follows. The sequences were aligned using mafft v. 7.475 (*35*) in --localpair mode and trimmed with trimAl v. 1.4.1 (*36*) (with -gt 0.9), and the phylogeny was reconstructed using iqtree2 v. 2.1.2 (*37*) with 1000 ultrafast bootstrap replicates (*38*). The tree was outgroup-rooted.

Structure-based alignment

Representative CCRs were aligned with 3D-coffee from t_coffee v.13.45.0.4846264 (methods sap_pair, mustang_pair, t_coffee_msa, and probcons_msa) (*39*). Transmembrane regions in ChRmine [Protein Data Bank (PDB): 7W9W] were predicted with the PPM web server (*40*).

Molecular biology and cell culture

Coding DNA sequences of HcKCR1 (MZ826862), HcKCR2 (MZ826861), WlChR1 and B1ChR2 (human codon adapted, synthesized by GenScript and accessible on GenBank via OP710241 and OP710242, respectively), and ChRmine (provided by K. Deisseroth) were fused to a Kir2.1 membrane targeting sequence, an mScarlet, mCerulean, or eYFP (enhanced yellow fluorescent protein) fluorophore, and an ER-Export signal and cloned either into a pCDNA3.1 vector behind a cytomegalovirus promotor for basic characterization in ND7/23 cells (ECACC 92090903 were purchased from Sigma-Aldrich) or into a pAAV backbone behind a human Synapsin promoter for virus production and expression in neurons. Site-directed mutagenesis was performed using the QuikChange Site-Directed Mutagenesis Kit (Agilent Technologies, Santa Clara, CA) according to the manufacturer′s instructions using primers provided in table S1. Expression in ND7/23 cells was performed as previously described (*41*). ND7/23 cells were cultured at 5% CO_2 and 37°C in Dulbecco′s minimal essential medium supplemented with 5% fetal bovine serum, 1 μM all-*trans*-retinal, and penicillin-streptomycin (100 μg/ml; Biochrom, Berlin, Germany). Cells were seeded on poly-lysin–coated coverslips at a concentration of 0.75×10^5 cells/ml and transiently transfected using the FuGENE HD Transfection Reagent (Promega, Madison, WI) 28 to 48 hours before measurement.

Whole-cell patch clamp in ND7/23 cells

Patch pipettes were prepared from borosilicate glass capillaries (G150F-3, Warner Instruments, Hamden, CT) using a P-1000 micropipette puller (Sutter Instruments, Novato, CA) and were subsequently fire-polished. Pipette resistance was 1.5 to 2.5 megohms. A 140 mM NaCl agar bridge served as a reference (bath) electrode. In whole-cell recordings, membrane resistance was typically >1 gigohm, while access resistance was below 10 megohms. Pipette capacity, series resistance, and cell capacity compensation were applied. All experiments were carried out at 23°C. Signals were amplified and filtered at 2 kHz, digitized at 10 kHz (DigiData1400), and acquired using Clampex 10.4 software (all from Molecular Devices, Sunnyvale, CA). Continuous monochromatic light was generated using a Polychrome V light source (TILL Photonics, Planegg, Germany) coupled into the Axiovert 100 microscope (Carl Zeiss) and delivered to the sample using a 90/10 beamsplitter (Chroma, Bellows Falls, VT). Light exposure was controlled by VS25 and VCM-D1 shutter systems (Vincent Associates, Rochester, NY). Light intensities were adjusted either manually by different neutral density filters or by a motorized filter wheel for equal photon densities in action spectra. Light intensities were measured in the sample plane with a calibrated P9710 optometer (Gigahertz Optik, Türkenfeld, Germany) with 3.7 mW/mm^2 at 470 nm and 2.7 mW/mm^2 at 530 nm for standard measurements. The illuminated field of the W Plan-Apochromat 40×/1.0 differential interference contrast (DIC) objective was 0.066 mm^2 (Carl Zeiss, Jena, Germany).

Extracellular solutions were replaced manually by adding at least 5 ml of the respective buffer to the recording chamber (500-μl chamber volume), while a Ringer Bath Handler MPCU (Lorenz Messgerätebau, Katlenburg-Lindau, Germany) maintained a constant bath level. Standard bath solutions contained 110 mM NaCl, 1 mM KCl, 2 mM $CaCl_2$, 2 mM $MgCl_2$, and 10 mM Hepes at pH_e 7.2 (with glucose added up to 310 mOsm). Standard pipette solutions contained 110 mM potassium-D-gluconate, 1 mM NaCl, 2 mM $CaCl_2$, 2 mM $MgCl_2$, 10 mM EGTA, and 10 mM Hepes at pH_i 7.2 (glucose was added up to 290 mOsm). For ion selectivity measurements, extracellular NaCl was replaced by 110 mM KCl or 110 mM N-methyl-D-glucamine chloride (NMDGCl).

I(*E*)-curves were measured from −80 to +40 mV in 20-mV steps with liquid junction potential (LJP)–corrected holding voltages and 500-ms illumination. Action spectra were recorded with 110 mM Na_e^+, 10-ms illumination, and reduced light intensities at either 0 mV for K^+-selective channels and mutants or −60 mV for HcKCR1 mutants that lost K^+ selectivity. Light titrations of KCR channels were recorded at 0 mV with 500-ms illumination.

ND7/23 measurements were analyzed using the Clampfit 10.7 software (Molecular Devices, Sunnyvale, CA), Microsoft Excel, and Origin 2020 (OriginLab, Northampton, MA). Photocurrent traces were baseline-corrected, filtered, and reduced in size for display purposes. Photocurrents were normalized to peak photocurrents at −40 mV and 110 mM K_e^+, and action spectra were fitted using a parametric Weibull function:with

$$y = y_0 + A \cdot \left(\frac{w_2 - 1}{w_2}\right)^{\left(\frac{1 - w_2}{w_2}\right)} \cdot S^{(w_2 - 1)} \cdot e^{\left(-S^{w_2} + \frac{w_2 - 1}{w_2}\right)}$$

$$\text{with } S = \frac{x - x_c}{w_1} + \left(\frac{w_2 - 1}{w_2}\right)^{\left(\frac{1}{w_2}\right)}$$

and the estimated parameters A, y_0, w_1, w_2, and x_c. Peak photocurrents represent the maximal photocurrent during the first 50 ms of illumination. The time point of peak conductance might vary for different voltages especially for channels that feature different open states and changes in ion selectivity during continuous illumination.

Confocal microscopy in ND7/23 cells and aCMs

ND7/23 cells

Confocal images were acquired using a FluoView1000 (Olympus, Tokyo, Japan) confocal laser scanning microscope with a UPlanSApo 60× numerical aperture (NA) 1.2 water-immersion objective (Olympus, Tokyo, Japan). mScarlet was excited using a 559-nm diode pumped solid state (DPSS) laser (2% transmissivity), mCerulean was excited using a 440-nm diode laser (10% transmissivity), and eYFP was excited using an argon laser (3% transmissivity).

Both the membrane fluorescent density (brightness/area) and the fluorescent density within the cell were calculated from equatorial slices after background subtraction. The membrane was defined as the outermost layer of the cell, and the targeting was then evaluated as the fluorescence membrane density in the membrane divided by the intracellular fluorescence density. This calculation yields a value below one if the fluorescence is higher inside the cell and above one if the membrane is brighter.

Atrial cardiomyocytes

Cells transfected to express WichR-mScarlet were imaged using an inverted confocal microscope (TCS SP8 X, Leica Microsystems, Wetzlar, Germany) using a 40× water objective (HC PL APO 40×/1,10 W CORR CS2, Leica Microsystems). DAPI (4′,6-diamidino-2-phenylindole) was excited using a 405-nm laser diode, and mScarlet was excited using a 569-nm line from the white light laser. The pinhole opening was set to four Airy units for overview

images and to one Airy unit for high-resolution images. Emission light was recorded using hybrid detectors and appropriate detection windows.

Preparation and electroporation of organotypic hippocampal slices

All animal procedures were performed in accordance with French law and guidelines of Directive 2010/63/EU and institutional guidelines on the care and use of laboratory animals. Organotypic hippocampal slices were prepared from P5/P8 C57BL/6J mouse pups as described by Gee *et al.* (*42*). In brief, dissection of hippocampi was carried out in ice-cold dissection solution composed of 248 mM sucrose, 26 mM $NaHCO_3$, 10 mM glucose, 4 mM KCl, 5 mM $MgCl_2$, 1 mM $CaCl_2$, 2 mM kynurenic acid, and 0.001% phenol red saturated with 95% O_2/5% CO_2. Transverse sections of hippocampi (400 μm thick) were sliced using a McIlwain tissue chopper with double-edge stainless steel razor blades. Morphologically intact slices were carefully transferred using a plastic transfer pipette onto small pieces of polytetrafluorethylene (PTFE) membrane (Millipore FHLP04700) on membrane inserts (Millicell PICM0RG50) in prewarmed culture medium. The slices were cultured at 37°C and 5% CO_2 in a culture medium consisting of 80% minimal essential medium and 20% heat-inactivated horse serum supplemented with 1 mM L-glutamine, insulin (0.01 mg/ml), 0.00125% ascorbic acid D-glucose, 14.5 mM NaCl, 2 mM $MgSO_4$, and 1.44 mM $CaCl_2$; no antibiotics were added to the culture medium. Three to four slices were cultured on one insert, and every 3 days, the medium was partially exchanged with prewarmed fresh medium.

Bulk electroporations were performed with endotoxin-free plasmid preparations (> 0.9 μg/μl) using the Y-unit of 4D-Nucleofector (Lonza Bioscience). Both HcKCR1 and WiChR were subcloned into a pAAV backbone and expressed as fusion proteins tagged with a fluorophore under a human syn1 promoter. At 3 to 4 days in vitro, the hippocampal slice was placed in a well of a 24-well culture plate (Nunc), and 10 μg of plasmid DNA in a volume of 25 to 30 μl of AD1 solution (Lonza Bioscience) was put as a drop on the slice. After an incubation period of 20 min at 37°C, prewarmed AD1 solution was added to a final volume of 360 μl. The 24-well dipping electrode array (Lonza Bioscience) was carefully placed onto the 24-well culture plate to avoid air bubbles, which could disrupt the electroporation, immediately followed by the electroporation using program CM-158 of the 4D-Nucleofector Y Unit. The slices were used for electrophysiology recordings 6 to 10 days after electroporation.

Holographic microscope for 2P excitation

The system, for holographic light shaping (*2*), is schematically represented in fig. S11A. It was custom-built around a commercial upright microscope (Zeiss, Axio Examiner.Z1). An efficient holographic stimulation was based on the use of a low repetition rate amplified fiber laser, providing ~300-fs pulses at 500-kHz rate with a 1030-nm wavelength (Satsuma, Amplitude Lasers; total output power, 10 W). The laser beam, after a first beam expander (f1 = 50 mm; f2 = 200 mm), was directed on a spatial light modulator (SLM) (LCOS-SLM X13138-07, Hamamatsu Photonics, 1280 × 1024 pixels, 12.5-μm pixel size). Then, a couple of 4f telescopes (f1 = 750 mm and f2 = 250 mm; f3 = 50 mm and f4 = 250 mm) projected the SLM plane to the pupil of a 20× 1.0 NA objective (Zeiss, W Plan-Apochromat 20×/1.0 DIC). The SLM was controlled by custom-made C++ based software (*43*) that uses a variation of the Gerchberg and Saxton algorithm (*44*) to calculate a phase-hologram to modulate the laser beam and to generate an arbitrary illumination shape at the sample plane. For single-neuron excitation, a 12-μm-diameter circular spot was generated. A physical blocker was placed between the two lenses of the first 4f system to avoid the zero order of diffraction reaching the sample. For alignment and calibration, holographic patterns were projected on a thin spin-coated rhodamine fluorescent layer, and the induced fluorescence was visualized on a complementary metal-oxide semiconductor (CMOS) camera (Hamamatsu ORCA-5G). To reconstruct a full 3D profile of the illumination spot (as reported in fig. S11), a second inverted microscope was built in transmission geometry and different axial sections of the spot were imaged on a second bottom camera while translating axially the upper objective [as described in (*44*)]. Fast shuttering and power control of illumination pulses were achieved using a built-in acousto-optic modulator that was controlled with the Digitizer (DigiData 1440, Molecular Devices) to ensure synchronization with the electrophysiology recordings. The microscope also enables widefield fluorescence imaging using a multi-LED (light-emitting diode) illumination system (pE-4000, CoolLed) and a DIC-transmitted imaging.

For whole-cell patch-clamp recordings, the microscope is equipped with a micromanipulator (Junior XR, Luigs and Neuman); signals were amplified and digitized using AxoPatch 700B (Molecular Devices) and DigiData 1440A (Molecular Devices), while data were acquired using Clampex (Molecular Devices).

2P electrophysiology recordings in organotypic slices

Recordings were performed 6 to 9 days after electroporation with transfected cells identified by their fluorescence. Patch pipettes were pulled from fire-polished capillaries with filament (outer diameter, 1.5 mm/inside diameter, 0.86 mm; World Precision Instruments) using a micropipette puller (P1000, Sutter Instruments). Pipettes with a resistance in a range from 3 to 6 megohms were filled with a K-gluconate–based intracellular solution: 135 mM K-Gluc, 10 mM Hepes, 10 mM Na-phosphocreatine, 4 mM KCl, 4 mM Mg- adenosine triphosphate, and 0.3 mM Na_2-guanosine triphosphate; 290 mOsm. Extracellular solution was composed of 125 mM NaCl, 26 mM $NaHCO_3$, 1.25 mM NaH_2PO_4, 25 mM D-glucose, 2.5 mM KCl, 1.5 mM $CaCl_2$, 1 mM $MgCl_2$, and 0.5 mM ascorbic acid (310 mOsm); continuously bubbled with carbogen (pH 7.4); and perfused at a rate of 1.5 to 2.5 ml/min [room temperature (RT)]. The LJP was calculated to be −17.7 mV according to the stationary Nernst-Planck equation (*45*), and it was corrected after acquisition for all recordings. The Nernst potential for K^+ is −103 mV, while that for sodium is +48 mV in these conditions.

After establishing the whole-cell configuration in voltage clamp mode, the quality of the patch was checked and access resistance was continuously monitored during and after the recording (voltage clamp); if access resistance rose above 45 megohms, recordings were discarded. After switching to current-clamp mode, bridge balance compensation was performed with the internal circuits of the amplifier, and neuronal parameters like resting potential, input resistance, and rheobase were determined (fig. S12B). During the recording, constant holding currents (between −50 and +50 pA)

were injected (if necessary) to keep the neurons at a comparable membrane potential between −75 and −80 mV.

For the 2P stimulation, a circular holographic spot of ≃12 μm diameter (fig. S12B) was generated aiming at the cell body of the patched neuron. Stimulation light powers were measured every recording day out of the microscope objective (PM160 power meter, Thorlabs), fitted within the range of interest, and used to calculate the exact photostimulation intensity. A typical average spot size of 126 μm^2 was determined from multiple images of the spot fluorescence on a thin rhodamine layer and used to calculate the power densities reported in the respective figures.

Square current injections of 1-s duration were increased in 10-pA steps per sweep, starting with hyperpolarizing injections, with a 5-s pause between sweeps. The duration of the current injection was divided into the first 250 ms (before illumination), 500 ms (during illumination), and 250 ms (after illumination) for analysis. Illumination was either continuous for the whole 500-ms pulses or a sequence of 5-ms pulses at different frequencies (30 to 35 $\mu W/\mu m^2$). The firing rates were determined during these intervals and normalized to the firing rate during the first 250 ms. The firing rates were extracted for each neuron at current injections of 50 and 100 pA above the respective rheobase of the neuron, with the rheobase determined as the current injection where the first spike in the first or last 250 ms (no illumination) occurred. After extraction, the normalized firing rates were averaged and plotted as mean ± SD. Control recordings were performed and analyzed in the same way but without any light application in the middle 500 ms.

For recording the reversal from light-induced hyperpolarization to depolarization, square current injections were increased in 10-pA steps around the reversal, and continuous illumination at saturating intensities (30 to 35 $\mu W/\mu m^2$) was switched on after 250 ms. Light-induced ΔV_{mem} was extracted as the difference between V_{mem} before illumination and at 150 ms into the illumination. The value for the reversal was extracted by linear interpolation on the individual recordings and then averaged over all cells.

For the comparison of the effectiveness of inhibition, somatic ramp current injections (800 ms) with continuous illumination of rising power densities were applied (5 s waiting between sweeps). The amplitudes of the ramp were constant for each individual neuron and chosen to give 10 to 20 APs in the dark, respectively (between 75 and 500 pA). The timing of the AP was extracted at the peak amplitude of the spike, and the delay was calculated with respect to the first AP on the ramp injection without illumination. Afterward, the delay was normalized between no delay (0) and maximum delay (1, no spike on ramp). The resulting values were plotted against the power densities of the respective recording day and fitted with a five-parameter logistic function. Then, the values of the individual recordings were averaged. Data were analyzed using Clampfit, custom Python scripts, Easy Electrophysiology, and Origin 2021.

2P spectra

Spectra were recorded in ND7/23 cells plated and transfected with WiChR as described above (see the "Molecular biology and cell culture" section). Recordings were performed in a dedicated 2P setup equipped with a tunable high repetition rate laser (Coherent Discovery, 80 MHz) and with a light path for parallel illumination using a large Gaussian beam. The path contained a half-wave plate (Thorlabs, CCM1-PBS253/M) on a motorized rotation mount (Thorlabs, PRM1Z8) followed by a polarizing beam splitter (Thorlabs, PBS253) to control the laser intensity and a mechanical shutter (Thorlabs, SH05R/M) to gate the illumination, and the collimated Gaussian beam was then projected on the sample by a tube lens (ACT508-300-B, Thorlabs) and a water immersion Chromatic Abberation free Infinity Apochromat Near InfraRed objective (CFI APO NIR, ×40, 0.8 NA, Nikon). An iris, placed on the intermediate image plane before the tube lens, allowed to crop the beam and reduce the size of the illuminated region, resulting in a circular homogeneous spot on the sample with a diameter of ≃22 μm and a surface of 400 μm^2. For the recordings, we used low illumination powers ranging from 7.55 mW at 840 nm (0.019 $mW/\mu m^2$) to 5.74 mW at 1080 nm (0.014 $mW/\mu m^2$); powers were adjusted to achieve an equal photon flux (8.0 ± 0.1 *10^{25} photons s^{-1} m^{-2}) across all wavelengths. In addition, we measured the pulse width after the objective with an autocorrelator (Carpe, APE, Germany), and the width was adjusted to 130 fs (full width at half maximum, sech fit) across all wavelengths using a built-in pulse stretcher/compressor of the laser. For patch-clamp recordings, signals were amplified and digitized using AxoPatch 700B (Molecular Devices) and DigiData 1550B (Molecular Devices), while data were acquired using Clampex software (Molecular Devices).

To characterize the 2P response, we recorded the photocurrent in voltage clamp mode (V_{hold} = 0 mV) upon a 10-ms illumination. We used the same K-gluconate intracellular solution as described for the slice recordings and a HEPES-based extracellular solution: 135 mM NaCl, 12.5 mM D-glucose, 2.5 mM KCl, 2 mM $CaCl_2$, and 1 mM $MgCl_2$. We did not use perfusion; the LJP is 15.2 mV and was not corrected for the spectral recordings. We measured the photocurrents across the indicated wavelengths from 840 to 1080 nm in a random order. Because of the tuning of the laser and necessary adaptation of the power, there were at least 5 s between each sweep. For analysis, we fitted the first 3 ms of each photocurrent rise with a linear function and extracted the slope as the 2P response. Resulting values for each cell were normalized to the highest response and then averaged across all cells (n = 5). The resulting data were fitted with a parametric Weibull function as described for the 1P spectra above.

Viral injections and in vivo patch-clamp and photostimulation experiments

Animal experiments were performed in accordance with Directive 2010/63/EU of the European Parliament and of the Council of 22 September 2010 and the protocols approved (APAFIS#14267-201803261541580 v3) by the institutional ethics committee for animal research (CEEA005). Adult female or male mice (4 weeks old) of C57BL/6 background (Janvier Labs) were used in experiments.

Mice were anesthetized by using intraperitoneal injection of a ketamine-xylazine mixture (0.1 mg of ketamine plus 0.01 mg of xylazine per gram body weight) during stereotaxic injection of viral vectors (AAV9-hSyn-WiChR-TS-mScarlet-ER) and using isoflurane (2% for induction and 0.5 to 1% for experiment) during whole-cell patch-clamp experiments. AAV was generated by the Viral Core Facility of the Charité–Universitätsmedizin Berlin, Germany.

To express WiChR at the layer 2/3 of mouse primary visual cortex, 1 μl of viral vectors (1:5 dilution from a titer of 2 × 10^{12} vg/ml) was infused via a cannula at 250 μm at a speed of 90 nl/

min through a craniotomy over primary visual cortex (3.5 mm caudal from bregma, 2.5 mm lateral from midline). To perform acute experiments, the mouse was head-fixed by attaching the skull to a metal plate. A circular craniotomy of 2 mm in diameter was made over the primary visual cortex, and the dura mater was removed. To dampen the tissue movement during experiment, agarose of 0.5 to 2% and a cover glass were applied on top of the craniotomy.

Whole-cell recordings in WiChR-expressing neurons at the layer 2/3 of anesthetized mouse visual cortex were obtained under the visual guidance of 2P scanning imaging by using the custom-built optical system equipped with a Ti:sapphire laser (Cameleon Vision II, Coherent) and a 16× water-immersion objective (CF175 LWD, Nikon). The 2P scanning imaging system was similar to that described in (*46*), and mScarlet labeling in opsin-expressing cells was visualized by using a laser wavelength of 960 to 980 nm.

Patch pipettes of 5- to 8-megohm tip resistance were fabricated from borosilicate glass by using a microelectrode puller (Sutter Instruments). The internal solution was the same as for the slice recordings. The external Ringer's solution, which was applied on top of the craniotomy, contained 145 mM NaCl, 5.4 mM KCl, 10 mM Hepes, 1 mM $MgCl_2$, and 1.8 mM $CaCl_2$. Membrane potential recordings were acquired by using current-clamp configuration and were corrected for an LJP of 11.9 mV. Patch-clamp recordings were performed by using the Multiclamp 700B amplifier (filtered at 6 kHz) and the Digidata 1550A digitizer (digitized at 20 kHz), which were controlled by the pCLAMP10 software (Molecular Devices).

On the custom-built system for in vivo photostimulation, the stimulation path was equivalent to that described in (*47*). It was based on the use of an amplified fiber laser at 1030 nm, similar to the one used for in vitro recordings, (Satsuma HP, Amplitude Systems; repetition rate, 500 kHz; maximum average power, 50 W; pulse width ≃300 fs), and the beam was modulated by a combination of a static phase mask (Double Helix Optics, Colorado), a reconfigurable SLM (LCOS-SLM, X10468-07, Hamamatsu Photonics), and a diffraction grating for temporal focusing (*48*). The resulting illumination spot was a circular holographic pattern of 12-μm lateral diameter and ≃14-μm axial confinement, focused through a 16× 0.8 NA water immersion objective (N16XLWD-PF, Nikon). The stimulation protocols and the SLM were controlled by using a Matlab software (MathWorks) and a custom-designed C++-based software Wavefront IV (*43*). The stimulation path was combined with the 2P scanning imaging system mentioned above.

Differentiation and culturing of aCM

We used a hiPSC line obtained from a healthy male donor via the American Type Culture Collection (catalog no. CRL-2097 TM). Ethical approval for using the hiPSCs was provided via 108-88-1 within the project SAF2009-07965 funded by the "Ministerio economía y competitividad," Spain. This line was generated from foreskin fibroblasts using a lentiviral vector expressing the *OCT4*, *NANOG*, *LIN28*, and *SOX2* genes (*49*). Different clones were obtained and validated using the following assays: alkaline phosphatase, surface marker expression, pluripotency gene expression, transgene silencing, proviral integration, and in vitro differentiation.

Next, direct differentiation of hiPSC into aCMs was performed via modulation of the Wnt and retinoic acid signaling pathways, as previously described (*50*). In brief, differentiation was initiated at 80 to 90% confluency on Vitronectin XF–coated plates (STEMCELL Technologies, Vancouver, Canada) with medium composed of RPMI 1640 with GlutaMAX and Hepes, 2% B-27 Supplement Minus Insulin, L-ascorbic acid 2-phosphate (0.2 mg/ml), and 6 μM CHIR99021 (STEMCELL Technologies) for the first 48 hours. On day 2, medium was replaced with a medium composed of RPMI 1640 with GlutaMAX and Hepes, 2% B-27 supplement, L-ascorbic acid 2-phosphate (0.2 mg/ml), and 5 μM IWP4 (inhibitor of Wnt/β-catenin signaling, STEMCELL Technologies) for 48 hours. From day 4, cells were maintained with cardio culture medium composed of RPMI 1640 with GlutaMAX and Hepes, 2% B-27 supplement, and L-ascorbic acid 2-phosphate (0.2 mg/ml). For differentiation into aCM-like cells, 1 μM retinoic acid (Sigma-Aldrich, Burlington, MA, USA) was supplemented on days 3 to 8 of differentiation.

Last, differentiated cultures were digested with StemPro Accutase on day 15 and replated at a density of 200,000 cells/cm^2 on Vitronectin XF–coated plates. Metabolic CM selection was performed for 5 days using cardio selection medium composed of RPMI 1640 without glucose, 2% B-27 supplement, L-ascorbic acid 2-phosphate (0.2 mg/ml), and 4 mM lactate (Sigma-Aldrich). Afterward, iPSC-derived CMs were cultured in cardio culture medium until day 25 for further maturation and then digested and replated on coverslips at a density of 100,000 cells/cm^2 for the experiments. After 3 days of recovery, cells were transiently transfected using the Lipofectamine Stem Transfection Reagent according to the manufacturer's protocol. If not stated otherwise, reagents were obtained from Thermo Fisher Scientific (Waltham, MA, USA).

Intracellular AP recordings of aCM

Two days after transfection, cells seeded on coverslips were placed in a perfusion chamber (RC-26G; Warner Instruments, Holliston, MA, USA) under constant flow (2 ml per min) controlled with a peristaltic pump (Masterflex L/S Easy-Load II Pump, Avantor, Radnor, PA, USA) at 35 ± 2°C. Bath solution was an oxygenated Hepes-buffered solution (140 mM NaCl, 5.5 mM KCl, 10 mM Hepes, 1 mM $MgCl_2$, 10 mM glucose, and 1.8 mM $CaCl_2$). Cells sitting in large multilayered clusters were impaled with microelectrodes that had a resistance of 15 to 20 megohms obtained by pulling glass capillaries (Clark Borosilicate Standard Wall with Filament; outer diameter, 1.00; inside diameter, 0.58; length, 100 mm) using a Sutter P-97 micropipette puller (Sutter Instrument, Novato, CA, USA). Microelectrodes were filled with 3 M KCl and connected to a bridge amplifier (BA-01X, NPI Electronic, Tamm, Germany) via an Ag-AgCl electrode. The reference electrode placed in the bath was an Ag-AgCl pellet connected to a wire electrode (E205, diameter 1.0 mm; Harvard Apparatus, Holliston, MA, USA). Micropositioning of the electrode was achieved using a micromanipulator (TSC, Sensapex, Oulu, Finland) and controlled using an inverted microscope (IX70, Olympus, Tokyo, Japan). Sharp electrode recordings were performed in a blinded manner independent of fluorescence levels at the point of impalement. Recordings were acquired at 50 kHz and filtered at 10 kHz using a LabView (National Instruments, Austin, TX, USA). Light was provided by a 460-nm LED using a 460/2-nm band-pass excitation filter, yielding a maximum light intensity of 3 mW/mm^2 in the object plane. Light pulses were controlled with custom-built hardware and software (Essel Research, Toronto, Canada). An average of 450 APs were recorded per impalement site. APs were analyzed using a custom Python script (*51*) and plotted using Prism 9 (GraphPad Software,

San Diego, CA, USA). All sharp electrode recordings with maximum diastolic potentials below −40 mV that showed stable APs were included for further analysis. As an alternative, to sharp electrode recordings, we performed whole-cell patch-clamp recordings on aCMs following a previously described protocol (*52*) but using a modified extracellular solution containing 4.5 mM KCl. After functional experiments, aCM were fixed with 4% paraformaldehyde in phosphate-buffered saline (PBS) for 10 min at RT. Fixed samples were washed three times in PBS and stored at 4°C before further processing. Samples were incubated in PBS with 0.1% Tween 20 and 300 nM DAPI (nuclear stain) for 10 min at RT, washed three times in PBS for 10 min, transferred to 35-mm glass-bottom μ-Dishes (ibidi, Gräfelfing, Germany), and immediately used for confocal imaging.

Video recordings of aCM

Two days after transfection, cells were transferred to a stage-top incubator (STXF/STX-CO2O2, Tokai Hit, Fujinomiya, Japan), maintaining a humidified atmosphere at 5% CO_2 and 37°C, and were allowed to equilibrate for 20 min. The incubator was mounted onto an inverted microscope (DMi8, Leica Microsystems) equipped with a mercury lamp (HXP 120V, Leistungselektronik Jena, Jena, Germany) coupled via a light guide to the epifluorescence port. The activation light was filtered by a 470/40-nm excitation filter and reflected by a 495-nm dichroic mirror, resulting in a light intensity of 0.2 mW/mm^2 in the object plane. The shutter was controlled via an externally provided transistor-transistor logic pulse. Transmission light passed a 640/20-nm filter, and an additional 630/75-nm emission filter was used in front of the camera (Zyla 5.5 ZsCMOS, Andor–Oxford Instruments, Abingdon, UK). Transmission images were recorded via a 10× objective at 20 Hz with 50-ms exposure time and 2 × 2 binning at 500 × 500 pixels using the AndorSolis software (Andor–Oxford Instruments). aCM contractions were analyzed on the basis of their movement in the acquired videos using an in-house script in MatLab2019 [script provided by R. Emig, IEKM; (*53*)]. Briefly, the frame in which the cells were most relaxed was chosen manually and set as a reference. The difference of each individual frame from the reference frame was calculated by pixel-wise subtraction of intensities. The mean difference per frame is referred to as dissimilarity score. All used scripts have been deposited on publicly accessible platforms.

Temperature simulations

The temporal distribution of the temperature rise reported in fig. S13 was calculated by solving the Fourier heat diffusion equation (*54*), considering the brain tissue as an infinite medium with isotropic and uniform thermal properties as described and experimentally verified before (*22*). For these simulations, light scattering in the tissue was neglected.

The reported temperature rise was calculated for $r = 0$, representing the center of the first holographic spot in the middle of the field of view. Additional spots were randomly added to the first one to maintain a relatively uniform distribution within the 100 μm × 100 μm surface.

3D structure prediction and system preparation for MD simulations

The HcKCR1, WiChR, and B1ChR2 3D models were generated using their full-length amino acid sequences with AlphaFold2 v.2.1.1 (*55*) with the full structural dataset running on a dedicated group server. On the basis of the sequence similarity to ChRmine, a trimeric assembly was chosen. For ChRmine, the trimeric cryo–electron microscopy structure was used (PDB-ID 7SFK) (*19*). Each protomer of HcKCR1, WlChR1, and B1ChR2 was equipped with a retinal cofactor bound to K233 in HcKCR1, K251 in WlChR1, and K232 in B1ChR2. Internal hydration was predicted using Dowser++ (*56*). The central pores of the HcKCR1, WiChR, B1ChR2, and ChRmine trimer were closed using 1,2-dimyristoyl-sn-glycero-3-phosphocholine (DMPC) molecules manually placed in PyMOL v.2.5.0 (Schrödinger, LLC). Accordingly, three lipids were positioned for HcKCR1, WiChR, and ChRmine, and six were positioned for B1ChR2. All systems containing the protein, internal waters, and central lipids were introduced into a homogeneous DMPC bilayer membrane, respectively, surrounded by water and neutralized using 150 mM KCl using CharmmGUI (*57*).

Classical MD simulations in CHARMM at constant pH

MD simulations were carried out using CHARMM version c42b1 (*58*) and openMM version 7.0rc1 (*59*). The MD simulation was computed under NPT conditions (number of particles n, pressure p and temperature T, are kept constant while the volume is allowed to change), using a 2-fs time step, a 303.15 K Langevin heat bath, the particle-mesh Ewald method for long-range electrostatics, and the CHARMM36 force field (*60*). Before and between the initial equilibration steps, the protonation of all titratable residues was adjusted on the basis of periodical Karlsberg2$^+$ predictions (*61*, *62*). For further production runs, combined pK_a-MD simulations were computed. During classical MD simulations, pK_a values were calculated periodically for 11 snapshots of each 10-ns production run using Karlsberg2+MD (*62*) to subsequently adapt the protonation pattern of the system pH dependently (pH 8). For all the KCR models, stable standard protonation was determined throughout the simulations. Moreover, the conformational integrity and side-chain flexibility of amino acids were controlled by computing geometrical root mean square deviation values for each amino acid using custom scripts in PyMOL v.2.5.0. Equilibrated AlphaFold2 models are provided in data S5.

pK_a calculations in Karlsberg2

In Karlsberg2$^+$, the holoprotein structure and ions within a 4-Å cutoff were explicitly included. The rest was substituted with continuum solvation and an implicit ion concentration of 100 mM. Single-structure pK_a calculations during the equilibration were performed using APBS (*63*) in a conformational space of three pH-adapted conformations (PACs), while the pK_a calculations based on MD simulations used the extracted snapshots and created only single PACs at pH 7. All PACs were generated using Karlsberg2$^+$ in a self-consistent cycle, including adjustment of protonation patterns of titratable amino acids and salt bridge opening according to either pH −10, 7, or 20.

Statistical analysis

Throughout the paper, data are shown as mean ± SD. In addition, individual data points are displayed. Number of replicates and statistical analysis (if performed) are mentioned in the respective figure legends. For randomization, we shuffled the order of measured constructs and conditions. Preestablished and semiautomatic analysis

pipelines did not permit dismissal of individual data points or experiments by the analyst.

Supplementary Materials

This PDF file includes:
Supplementary Text
Figs. S1 to S15
References

Other Supplementary Material for this manuscript includes the following:
Data S1 to S5
Movie S1
Table S1

View/request a protocol for this paper from *Bio-protocol*.

REFERENCES AND NOTES

1. V. Emiliani, E. Entcheva, R. Hedrich, P. Hegemann, K. R. Konrad, C. Lüscher, M. Mahn, Z. H. Pan, R. R. Sims, J. Vierock, O. Yizhar, Optogenetics for light control of biological systems. *Nat. Rev. Methods Primers* **2**, 55 (2022).
2. E. Ronzitti, C. Ventalon, M. Canepari, B. C. Forget, E. Papagiakoumou, V. Emiliani, Recent advances in patterned photostimulation for optogenetics. *J. Optics* **19**, 113001 (2017).
3. H. Harz, P. Hegemann, Rhodopsin-regulated calcium currents in *Chlamydomonas*. *Nature* **351**, 489–491 (1991).
4. A. Rozenberg, J. Oppermann, J. Wietek, R. G. Fernandez Lahore, R. A. Sandaa, G. Bratbak, P. Hegemann, O. Béjà, Lateral gene transfer of anion-conducting channelrhodopsins between green algae and giant viruses. *Curr. Biol.* **30**, 4910–4920.e5 (2020).
5. E. G. Govorunova, O. A. Sineshchekov, H. Li, Y. Wang, L. S. Brown, A. Palmateer, M. Melkonian, S. Cheng, E. Carpenter, J. Patterson, G. K. S. Wong, J. L. Spudich, Cation and anion channelrhodopsins: Sequence motifs and taxonomic distribution. *MBio* **12**, e0165621 (2021).
6. I. Ehrlich, S. Löhrke, E. Friauf, Shift from depolarizing to hyperpolarizing glycine action in rat auditory neurones is due to age-dependent Cl^- regulation. *J. Physiol.* **520**, 121–137 (1999).
7. R. A. Kopton, J. S. Baillie, S. A. Rafferty, R. Moss, C. M. Zgierski-Johnston, S. V. Prykhozhij, M. R. Stoyek, F. M. Smith, P. Kohl, T. A. Quinn, F. Schneider-Warme, Cardiac electrophysiological effects of light-activated chloride channels. *Front. Physiol.* **9**, 1806 (2018).
8. M. Mahn, L. Gibor, P. Patil, K. Cohen-Kashi Malina, S. Oring, Y. Printz, R. Levy, I. Lampl, O. Yizhar, High-efficiency optogenetic silencing with soma-targeted anion-conducting channelrhodopsins. *Nat. Commun.* **9**, 4125 (2018).
9. M. Mahn, M. Prigge, S. Ron, R. Levy, O. Yizhar, Biophysical constraints of optogenetic inhibition at presynaptic terminals. *Nat. Neurosci.* **19**, 554–556 (2016).
10. M. Mahn, I. Saraf-Sinik, P. Patil, M. Pulin, E. Bitton, N. Karalis, F. Bruentgens, S. Palgi, A. Gat, J. Dine, J. Wietek, I. Davidi, R. Levy, A. Litvin, F. Zhou, K. Sauter, P. Soba, D. Schmitz, A. Lüthi, B. R. Rost, J. S. Wiegert, O. Yizhar, Efficient optogenetic silencing of neurotransmitter release with a mosquito rhodopsin. *Neuron* **109**, 1621–1635.e8 (2021).
11. H. E. Kato, F. Zhang, O. Yizhar, C. Ramakrishnan, T. Nishizawa, K. Hirata, J. Ito, Y. Aita, T. Tsukazaki, S. Hayashi, P. Hegemann, A. D. Maturana, R. Ishitani, K. Deisseroth, O. Nureki, Crystal structure of the channelrhodopsin light-gated cation channel. *Nature* **482**, 369–374 (2012).
12. D. A. Doyle, J. M. Cabral, R. A. Pfuetzner, A. Kuo, J. M. Gulbis, S. L. Cohen, B. T. Chait, R. MacKinnon, The structure of the potassium channel: Molecular basis of K+ conduction and selectivity. *Science* **280**, 69–77 (1998).
13. H. Janovjak, S. Szobota, C. Wyart, D. Trauner, E. Y. Isacoff, A light-gated, potassium-selective glutamate receptor for the optical inhibition of neuronal firing. *Nat. Neurosci.* **13**, 1027–1032 (2010).
14. C. Cosentino, L. Alberio, S. Gazzarrini, M. Aquila, E. Romano, S. Cermenati, P. Zuccolini, J. Petersen, M. Beltrame, J. L. van Etten, J. M. Christie, G. Thiel, A. Moroni, Engineering of a light-gated potassium channel. *Science* **348**, 707–710 (2015).
15. Y. A. Bernal Sierra, B. R. Rost, M. Pofahl, A. M. Fernandes, R. A. Kopton, S. Moser, D. Holtkamp, N. Masala, P. Beed, J. J. Tukker, S. Oldani, W. Bönigk, P. Kohl, H. Baier, F. Schneider-Warme, P. Hegemann, H. Beck, R. Seifert, D. Schmitz, Potassium channel-based optogenetic silencing. *Nat. Commun.* **9**, 4611 (2018).
16. A. Vogt, A. Silapetere, C. Grimm, F. Heiser, M. Ancina Möller, P. Hegemann, Engineered passive potassium conductance in the KR2 sodium pump. *Biophys. J.* **116**, 1941–1951 (2019).
17. E. G. Govorunova, Y. Gou, O. A. Sineshchekov, H. Li, X. Lu, Y. Wang, L. S. Brown, F. St-Pierre, M. Xue, J. L. Spudich, Kalium channelrhodopsins are natural light-gated potassium channels that mediate optogenetic inhibition. *Nat. Neurosci.* **25**, 967–974 (2022).
18. E. G. Govorunova, O. A. Sineshchekov, J. L. Spudich, Structurally distinct cation channelrhodopsins from cryptophyte algae. *Biophys. J.* **110**, 2302–2304 (2016).
19. K. Tucker, S. Sridharan, H. Adesnik, S. G. Brohawn, Cryo-EM structures of the channelrhodopsin ChRmine in lipid nanodiscs. *Nat. Commun.* **13**, 4842 (2022).
20. K. E. Kishi, Y. S. Kim, M. Fukuda, M. Inoue, T. Kusakizako, P. Y. Wang, C. Ramakrishnan, E. F. X. Byrne, E. Thadhani, J. M. Paggi, T. E. Matsui, K. Yamashita, T. Nagata, M. Konno, S. Quirin, M. Lo, T. Benster, T. Uemura, K. Liu, M. Shibata, N. Nomura, S. Iwata, O. Nureki, R. O. Dror, K. Inoue, K. Deisseroth, H. E. Kato, Structural basis for channel conduction in the pump-like channelrhodopsin ChRmine. *Cell* **185**, 672–689.e23 (2022).
21. E. G. Govorunova, O. A. Sineshchekov, L. S. Brown, J. L. Spudich, Biophysical characterization of light-gated ion channels using planar automated patch clamp. *Front. Mol. Neurosci.* **15**, 976910 (2022).
22. A. Picot, S. Dominguez, C. Liu, I. W. Chen, D. Tanese, E. Ronzitti, P. Berto, E. Papagiakoumou, D. Oron, G. Tessier, B. C. Forget, V. Emiliani, Temperature rise under two-photon optogenetic brain stimulation. *Cell Rep.* **24**, 1243–1253.e5 (2018).
23. O. A. Sineshchekov, E. G. Govorunova, H. Li, J. L. Spudich, Bacteriorhodopsin-like channelrhodopsins: Alternative mechanism for control of cation conductance. *Proc. Natl. Acad. Sci. U.S.A.* **114**, E9512–E9519 (2017).
24. Y. Zhou, J. H. Morais-Cabral, A. Kaufman, R. Mackinnon, Chemistry of ion coordination and hydration revealed by a K^+ channel-Fab complex at 2.0 Å resolution. *Nature* **414**, 43–48 (2001).
25. S. Oh, F. Marinelli, W. Zhou, J. Lee, H. J. Choi, M. Kim, J. D. Faraldo-Gómez, R. K. Hite, Differential ion dehydration energetics explains selectivity in the non-canonical lysosomal K^+ channel TMEM175. *eLife* **11**, e75122 (2022).
26. H. Dana, Y. Sun, B. Mohar, B. K. Hulse, A. M. Kerlin, J. P. Hasseman, G. Tsegaye, A. Tsang, A. Wong, R. Patel, J. J. Macklin, Y. Chen, A. Konnerth, V. Jayaraman, L. L. Looger, E. R. Schreiter, K. Svoboda, D. S. Kim, High-performance calcium sensors for imaging activity in neuronal populations and microcompartments. *Nat. Methods* **16**, 649–657 (2019).
27. J. Akerboom, N. C. Calderón, L. Tian, S. Wabnig, M. Prigge, J. Tolö, A. Gordus, M. B. Orger, K. E. Severi, J. J. Macklin, R. Patel, S. R. Pulver, T. J. Wardill, E. Fischer, C. Schüler, T. W. Chen, K. S. Sarkisyan, J. S. Marvin, C. I. Bargmann, D. S. Kim, S. Kügler, L. Lagnado, P. Hegemann, A. Gottschalk, E. R. Schreiter, L. L. Looger, Genetically encoded calcium indicators for multi-color neural activity imaging and combination with optogenetics. *Front. Mol. Neurosci.* **6**, 2 (2013).
28. Y. Zhao, S. Araki, J. Wu, T. Teramoto, Y. F. Chang, M. Nakano, A. S. Abdelfattah, M. Fujiwara, T. Ishihara, T. Nagai, R. E. Campbell, An expanded palette of genetically encoded Ca^{2+} indicators. *Science* **333**, 1888–1891 (2011).
29. F. Noguchi, G. Tanifuji, M. W. Brown, K. Fujikura, K. Takishita, Complex evolution of two types of cardiolipin synthase in the eukaryotic lineage stramenopiles. *Mol. Phylogenet. Evol.* **101**, 133–141 (2016).
30. M. G. Grabherr, B. J. Haas, M. Yassour, J. Z. Levin, D. A. Thompson, I. Amit, X. Adiconis, L. Fan, R. Raychowdhury, Q. Zeng, Z. Chen, E. Mauceli, N. Hacohen, A. Gnirke, N. Rhind, F. di Palma, B. W. Birren, C. Nusbaum, K. Lindblad-Toh, N. Friedman, A. Regev, Full-length transcriptome assembly from RNA-seq data without a reference genome. *Nat. Biotechnol.* **29**, 644–652 (2011).
31. S. R. Eddy, Accelerated profile HMM searches. *PLOS Comput. Biol.* **7**, e1002195 (2011).
32. S. F. Altschul, W. Gish, W. Miller, E. W. Myers, D. J. Lipman, Basic local alignment search tool. *J. Mol. Biol.* **215**, 403–410 (1990).
33. A. Bankevich, S. Nurk, D. Antipov, A. A. Gurevich, M. Dvorkin, A. S. Kulikov, V. M. Lesin, S. I. Nikolenko, S. Pham, A. D. Prjibelski, A. V. Pyshkin, A. V. Sirotkin, N. Vyahhi, G. Tesler, M. A. Alekseyev, P. A. Pevzner, SPAdes: A new genome assembly algorithm and its applications to single-cell sequencing. *J. Comput. Biol.* **19**, 455–477 (2012).
34. A. Rozenberg, A catalog of natural channelrhodopsins (2021); doi:10.5281/ZENODO.5749640.
35. K. Katoh, K. Misawa, K. I. Kuma, T. Miyata, MAFFT: A novel method for rapid multiple sequence alignment based on fast Fourier transform. *Nucleic Acids Res.* **30**, 3059–3066 (2002).
36. S. Capella-Gutiérrez, J. M. Silla-Martínez, T. Gabaldón, trimAl: A tool for automated alignment trimming in large-scale phylogenetic analyses. *Bioinformatics* **25**, 1972–1973 (2009).
37. B. Q. Minh, H. A. Schmidt, O. Chernomor, D. Schrempf, M. D. Woodhams, A. von Haeseler, R. Lanfear, IQ-TREE 2: New models and efficient methods for phylogenetic inference in the genomic era. *Mol. Biol. Evol.* **37**, 1530–1534 (2020).
38. D. T. Hoang, O. Chernomor, A. von Haeseler, B. Q. Minh, L. S. Vinh, UFBoot2: Improving the ultrafast bootstrap approximation. *Mol. Biol. Evol.* **35**, 518–522 (2018).
39. O. O'Sullivan, K. Suhre, C. Abergel, D. G. Higgins, C. Notredame, 3DCoffee: Combining protein sequences and structures within multiple sequence alignments. *J. Mol. Biol.* **340**, 385–395 (2004).

40. M. A. Lomize, I. D. Pogozheva, H. Joo, H. I. Mosberg, A. L. Lomize, OPM database and PPM web server: Resources for positioning of proteins in membranes. *Nucleic Acids Res.* **40**, D370–D376 (2012).
41. C. Grimm, J. Vierock, P. Hegemann, J. Wietek, Whole-cell patch-clamp recordings for electrophysiological determination of ion selectivity in channelrhodopsins. *J. Vis. Exp.* , 55497 (2017).
42. C. E. Gee, I. Ohmert, J. S. Wiegert, T. G. Oertner, Preparation of slice cultures from rodent hippocampus. *Cold Spring Harb. Protoc.* , (2017).
43. C. Lutz, T. S. Otis, V. DeSars, S. Charpak, D. A. DiGregorio, V. Emiliani, Holographic photolysis of caged neurotransmitters. *Nat. Methods* **5**, 821–827 (2008).
44. O. Hernandez, E. Papagiakoumou, D. Tanese, K. Fidelin, C. Wyart, V. Emiliani, Three-dimensional spatiotemporal focusing of holographic patterns. *Nat. Commun.* **7**, 11928 (2016).
45. M. Marino, L. Misuri, D. Brogioli, A new open source software for the calculation of the liquid junction potential between two solutions according to the stationary Nernst-Planck equation. arXiv:1403.3640 [physics.chem-ph] (14 March 2014).
46. I. W. Chen, E. Ronzitti, B. R. Lee, T. L. Daigle, D. Dalkara, H. Zeng, V. Emiliani, E. Papagiakoumou, In vivo submillisecond two-photon optogenetics with temporally focused patterned light. *J. Neurosci.* **39**, 3484–3497 (2019).
47. G. L. B. Spampinato, E. Ronzitti, V. Zampini, U. Ferrari, F. Trapani, H. Khabou, A. Agraval, D. Dalkara, S. Picaud, E. Papagiakoumou, O. Marre, V. Emiliani, All-optical inter-layers functional connectivity investigation in the mouse retina. *Cell Rep. Methods* **2**, 100268 (2022).
48. N. Accanto, C. Molinier, D. Tanese, E. Ronzitti, Z. L. Newman, C. Wyart, E. Isacoff, E. Papagiakoumou, V. Emiliani, Multiplexed temporally focused light shaping for high-resolution multi-cell targeting. *Optica* **5**, 1478–1491 (2018).
49. I. Ontoria-Oviedo, G. Földes, S. Tejedor, J. Panadero, T. Kitani, A. Vázquez, J. C. Wu, S. E. Harding, P. Sepúlveda, Modeling transposition of the great arteries with patient-specific induced pluripotent stem cells. *Int. J. Mol. Sci.* **22**, 13270 (2021).
50. L. Cyganek, M. Tiburcy, K. Sekeres, K. Gerstenberg, H. Bohnenberger, C. Lenz, S. Henze, M. Stauske, G. Salinas, W. H. Zimmermann, G. Hasenfuss, K. Guan, Deep phenotyping of human induced pluripotent stem cell-derived atrial and ventricular cardiomyocytes. *JCI Insight* **3**, e99941 (2018).
51. E. M. Wülfers, APAnalysis. Zenodo (2022); doi:10.5281/ZENODO.7127601.
52. M. C. Fernández, R. A. Kopton, A. Simon-Chica, J. Madl, I. Hilgendorf, C. M. Zgierski-Johnston, F. Schneider-Warme, Channelrhodopsins for cell-type specific illumination of cardiac electrophysiology. *Methods Mol. Biol.* **2191**, 287–307 (2021).
53. R. Peyronnet, iPS-CM contraction analysis. Zenodo (2022); doi:10.5281/ZENODO.7129072.
54. J.-B.-J. Fourier, *Théorie Analytique de la Chaleur* (F. Didot, 1822).
55. J. Jumper, R. Evans, A. Pritzel, T. Green, M. Figurnov, O. Ronneberger, K. Tunyasuvunakool, R. Bates, A. Žídek, A. Potapenko, A. Bridgland, C. Meyer, S. A. A. Kohl, A. J. Ballard, A. Cowie, B. Romera-Paredes, S. Nikolov, R. Jain, J. Adler, T. Back, S. Petersen, D. Reiman, E. Clancy, M. Zielinski, M. Steinegger, M. Pacholska, T. Berghammer, S. Bodenstein, D. Silver, O. Vinyals, A. W. Senior, K. Kavukcuoglu, P. Kohli, D. Hassabis, Highly accurate protein structure prediction with AlphaFold. *Nature* **596**, 583–589 (2021).
56. A. Morozenko, A. A. Stuchebrukhov, Dowser++, a new method of hydrating protein structures. *Proteins* **84**, 1347–1357 (2016).
57. S. Jo, T. Kim, V. G. Iyer, W. Im, CHARMM-GUI: A web-based graphical user interface for CHARMM. *J. Comput. Chem.* **29**, 1859–1865 (2008).
58. B. R. Brooks, C. L. Brooks III, A. D. Mackerell Jr., L. Nilsson, R. J. Petrella, B. Roux, Y. Won, G. Archontis, C. Bartels, S. Boresch, A. Caflisch, L. Caves, Q. Cui, A. R. Dinner, M. Feig, S. Fischer, J. Gao, M. Hodoscek, W. Im, K. Kuczera, T. Lazaridis, J. Ma, V. Ovchinnikov, E. Paci, R. W. Pastor, C. B. Post, J. Z. Pu, M. Schaefer, B. Tidor, R. M. Venable, H. L. Woodcock, X. Wu, W. Yang, D. M. York, M. Karplus, CHARMM: The biomolecular simulation program. *J. Comput. Chem.* **30**, 1545–1614 (2009).
59. P. Eastman, J. Swails, J. D. Chodera, R. T. McGibbon, Y. Zhao, K. A. Beauchamp, L. P. Wang, A. C. Simmonett, M. P. Harrigan, C. D. Stern, R. P. Wiewiora, B. R. Brooks, V. S. Pande, OpenMM 7: Rapid development of high performance algorithms for molecular dynamics. *PLOS Comput. Biol.* **13**, e1005659 (2017).
60. A. D. MacKerell Jr., D. Bashford, M. Bellott, R. L. Dunbrack, J. D. Evanseck, M. J. Field, S. Fischer, J. Gao, H. Guo, S. Ha, D. Joseph-McCarthy, L. Kuchnir, K. Kuczera, F. T. K. Lau, C. Mattos, S. Michnick, T. Ngo, D. T. Nguyen, B. Prodhom, W. E. Reiher, B. Roux, M. Schlenkrich, J. C. Smith, R. Stote, J. Straub, M. Watanabe, J. Wiórkiewicz-Kuczera, D. Yin, M. Karplus, All-atom empirical potential for molecular modeling and dynamics studies of proteins. *J. Phys. Chem. B* **102**, 3586–3616 (1998).
61. G. Kieseritzky, E. W. Knapp, Optimizing pKa computation in proteins with pH adapted conformations. *Proteins* **71**, 1335–1348 (2008).
62. T. Meyer, E. W. Knapp, pK_a values in proteins determined by electrostatics applied to molecular dynamics trajectories. *J. Chem. Theor. Comput.* **11**, 2827–2840 (2015).
63. E. Jurrus, D. Engel, K. Star, K. Monson, J. Brandi, L. E. Felberg, D. H. Brookes, L. Wilson, J. Chen, K. Liles, M. Chun, P. Li, D. W. Gohara, T. Dolinsky, R. Konecny, D. R. Koes, J. E. Nielsen, T. Head-Gordon, W. Geng, R. Krasny, G. W. Wei, M. J. Holst, J. A. McCammon, N. A. Baker, Improvements to the APBS biomolecular solvation software suite. *Protein Sci.* **27**, 112–128 (2018).
64. B. Langmead, S. L. Salzberg, Fast gapped-read alignment with Bowtie 2. *Nat. Methods* **9**, 357–359 (2012).
65. P. Danecek, J. K. Bonfield, J. Liddle, J. Marshall, V. Ohan, M. O. Pollard, A. Whitwham, T. Keane, S. A. McCarthy, R. M. Davies, H. Li, Twelve years of SAMtools and BCFtools. *Gigascience* **10**, giab008 (2021).
66. E. G. Govorunova, O. A. Sineshchekov, J. L. Spudich, Emerging diversity of channelrhodopsins and their structure-function relationships. *Front. Cell. Neurosci.* **15**, 800313 (2022).
67. R. Thakur, T. Shiratori, K. Ishida, Taxon-rich multigene phylogenetic analyses resolve the phylogenetic relationship among deep-branching stramenopiles. *Protist* **170**, 125682 (2019).
68. T. Shiratori, R. Thakur, K. Ishida, Pseudophyllomitus vesiculosus (Larsen and Patterson 1990) Lee, 2002, a poorly studied phagotrophic biflagellate is the first characterized member of stramenopile environmental clade MAST-6. *Protist* **168**, 439–451 (2017).
69. G. Leonard, A. Labarre, D. S. Milner, A. Monier, D. Soanes, J. G. Wideman, F. Maguire, S. Stevens, D. Sain, X. Grau-Bové, A. Sebé-Pedrós, J. E. Stajich, K. Paszkiewicz, M. W. Brown, N. Hall, B. Wickstead, T. A. Richards, Comparative genomic analysis of the 'pseudofungus' *Hyphochytrium catenoides*. *Open Biol.* **8**, 170184 (2018).
70. A. Cho, D. V. Tikhonenkov, E. Hehenberger, A. Karnkowska, A. P. Mylnikov, P. J. Keeling, Monophyly of diverse Bigyromonadea and their impact on phylogenomic relationships within stramenopiles. *Mol. Phylogenet. Evol.* **171**, 107468 (2022).

Acknowledgments: We thank S. Pouvreau for sharing slice electroporation protocol, Y. A. Bernal Sierra for constructive discussion on inhibition with light-controlled potassium channels, C. Y. Chan for technical support at the 2P in vivo setup, and A. Mohamed-Lafirdeen for the preparation of organotypic slices. Cardiac imaging data were recorded at the SCI-MED imaging facility at IEKM, University of Freiburg, Germany, and we thank R. Emig, E. M. Wülfers, and J. Madl for help with data acquisition and analysis. We thank all members of IEKM for critical discussion of cardiac experiments. **Funding:** This work was funded by Deutsche Forschungsgemeinschaft (DFG, German Research Foundation) SPP1926 425994138 (to P.H.) and 315193289 (to F.S.-W.), SFB 1315 (to P.H. and J.V.), and EXC-2049–390688087 (to J.V., L.T., and P.H.); Postdoc fellowship 442616457 (to C.G.) and Emmy-Noether fellowship 412853334 (to F.S.-W.); European Research Council Advanced Grant "Stardust," No. 767092 (to P.H. and E.P.); French National Research Agency ANR Holoptogen AAPG2019 (to V.E. and P.H.); European Research Council Advanced Grant "HOLOVIS-AdG" ERC2019-ADG-885090 (to V.E.); Israel Science Foundation grants 3592/19 and 3121/20 (to O.B.); and European Union's Horizon 2020 research and innovation programme under the Marie Skłodowska-Curie Actions (grant 860974, to M.C.). P.H. is a Hertie Professor supported by the Hertie Foundation; O.B. holds the Louis and Lyra Richmond Chair in Life Sciences. F.S.-W. and R.P. are members of the DFG-funded SFB1425. **Author contributions:** Conceptualization: P.H., J.V., E.P., and C.G. Bioinformatics: A.R. and O.B. Electrophysiology: J.V., E.P., S.A., and L.T. Neuronal studies: C.G., D.T., I.-W.C., and V.E. hiPSC studies: M.C., R.P., and F.S.-W. Simulations: E.P. and B.C.F. Confocal microscopy: A.G.C.S. and F.S.-W. Funding acquisition: P.H., O.B., V.E., F.S.-W., and J.V. Visualization: J.V., E.P., C.G., and A.R. Writing: J.V., C.G., E.P., A.R., F.S.-W., and P.H. with contributions from all authors. **Competing interests:** The authors declare that they have no competing interests. **Data and materials availability:** All data needed to evaluate the conclusions in the paper are present in the paper and/or the Supplementary Materials.

Submitted 3 July 2022
Accepted 28 October 2022
Published 9 December 2022
10.1126/sciadv.add7729